Title
STUDY OF NICKEL-TUNGSTEN ALLOY (Ni4W) WITH FIELD-ION-FIELD-EMISSION MICROSCOPY

Author
Lira-Olivares, Joaquin.

Publication Date
1970-12-01

UCRL-20330

c.2

STUDY OF NICKEL-TUNGSTEN ALLOY (Ni_4W) WITH FIELD-ION-FIELD-EMISSION MICROSCOPY

Joaquin Lira-Olivares
(M.S. Thesis)

December 1970

AEC Contract No. W-7405-eng-48

LAWRENCE RADIATION LABORATORY
UNIVERSITY of CALIFORNIA BERKELEY

UCRL-20330 c.2

DISCLAIMER

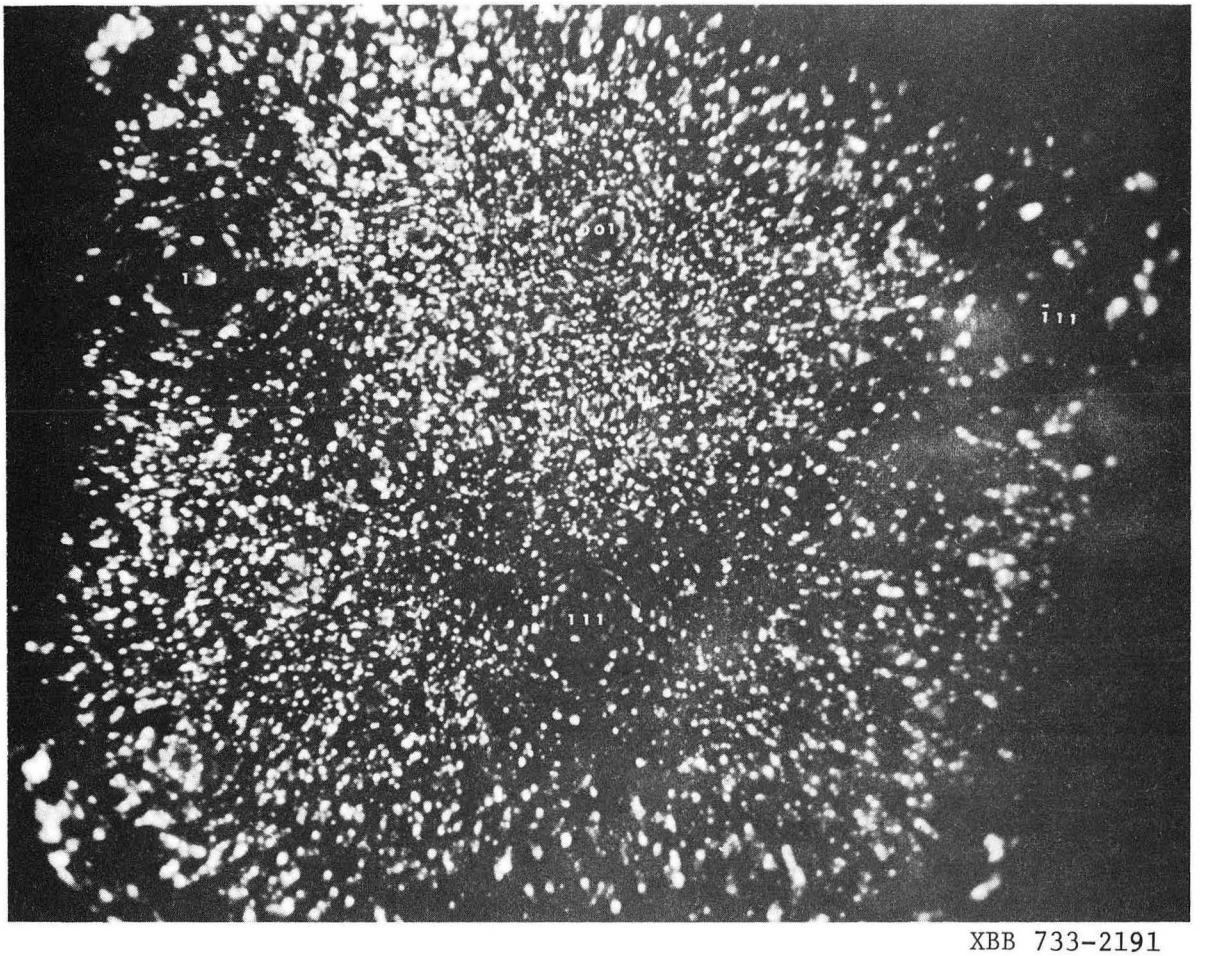

XBB 733-2191

Fig. 9.

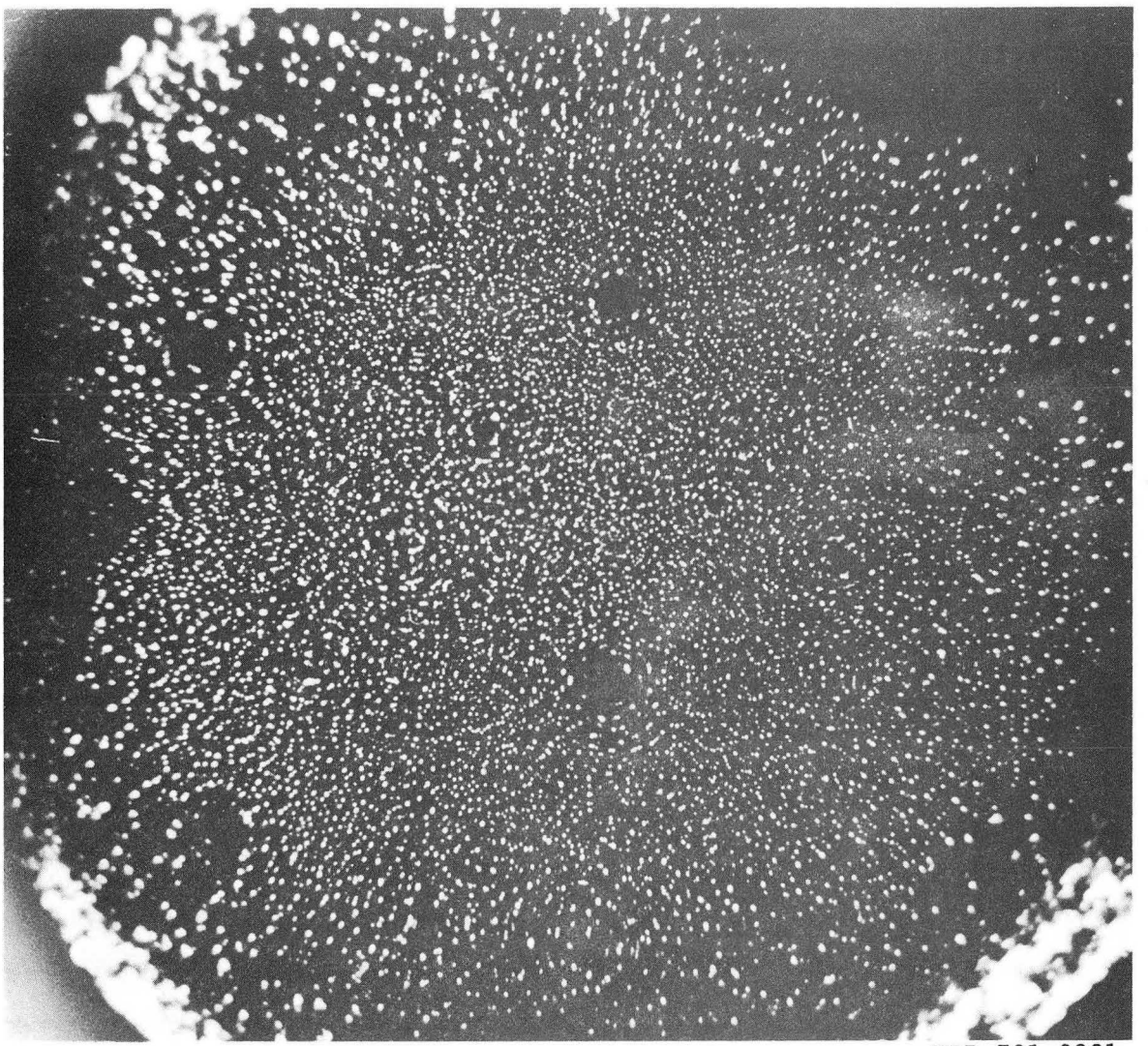

XBB 731-0021

Fig. 13.

CONTENTS

STUDY OF NICKEL-TUNGSTEN ALLOY (Ni_4W) WITH FIELD-ION-FIELD-EMISSION MICROSCOPY

Joaquín Lira-Olivares

Inorganic Materials Research Division, Lawrence Radiation Laboratory
Department of Materials Science and Engineering, College of Engineering
University of California, Berkeley, California

ABSTRACT

Field ion micrographs of pure metals and alloys usually show regions of different brightness. Some of these features have been satisfactorily explained. However, agreement is lacking as to origin of dark bands as they appear in nickel and some of its alloys.

The present work substantiates the existence of dark bands and clarifies the conditions necessary for their appearance in FIM images.

Field ionization micrographs of Ni_4W as quenched from 1300°C showed a dark zone pattern at 78°K that is similar to the patterns obtained for Ni and Ni_4Mo. A less conspicuous pattern was observed in the β phase of the same alloy at 4.2°K.

The dark band pattern was explained using a topographic model including preferential field evaporation at dark band regions of the specimen due to a higher work function at these regions.

The use of field emission microscopy in conjunction with field ion microscopy proved effective in making it possible to discard some of the previous hypotheses and in relating work function to dark band formation.

UNIVERSITY OF CALIFORNIA

Lawrence Berkeley Laboratory
Berkeley, California

Date: April 24, 1973

ERRATA

TO: All recipients of UCRL-20330

FROM: Inorganic Materials Research Div. and Technical Information Div.

SUBJECT: UCRL-20330, "Study of Nickel-Tungsten Alloy (Ni_4W) with Field-Ion-Field-Emission Microscopy," Joaquin Lira-Olivares, (Dec. 1970).

Please make the following corrections on subject report.

Page 2, line 9, reads: we have photoelectric emission and when by phonons we have thermionic It should read: we have photoelectric emission and when by heating we have thermionic Eq. (1), reads:

$$J = 6.2\times10^{-6} \frac{(\mu/\phi)^{1/2}}{Kf+\phi} \quad .....$$

It should read:

$$J = 6.2\times10^{-6} \frac{(\mu/\phi)^{1/2}}{F+\phi} \quad .....$$

Page 3, reads: expressed as electron volts/cm and J is amps/cm.^{2}

It should read: expressed as electron volts/cm and J is amp/cm;^{2} a is a slowly varying hyperbolic function that has been previously tabulated.[6]

Page 7, Eq. (9) reads: $\delta = 4r\beta(KT/Ve)^{1/2}$

It should read: $$\delta = \sqrt{4r\beta(KT/Ve)^2 + \left(\frac{4\beta^2 r\hbar^2}{2KMF}\right)^2}$$

Line 15, reads: voltage (V=KrF) and T is the absolute temperature.(4)

It should read: voltage (V=KrF) and T is the absolute temperature,(4) M is the atomic mass of the imaging gas and F is the external field.

Page 49, Fig. 9, replace with attached corrected figure.

Page 53, Fig. 13, replace with attached corrected figure.

1. INTRODUCTION

Direct observation of metallic surfaces with atomic or nearly atomic scale resolution has been made possible thanks to the invention of the field-ion microscope (FIM) and the field-emission microscope (FEM) by E. Müller.

Field-ion and field-emission microscopes are both projection microscopes where the image is formed by particles projecting radially from a sharp pointed needle-like specimen (500 Å to 2000 Å in diameter at the tip) and striking a fluorescent screen that can be photographed.

In the field-ion microscope the specimen is positively charged and gas at low pressure is allowed into the instrument's chamber (a typical pressure would be 10^{-4} torr). The image is formed by the positive gas ions produced near the specimen's surface, when electrons from the gas atoms tunnel into the specimen.

In the field emission microscope the image is formed by electrons escaping from the negatively charged specimen by quantum mechanical tunneling under the influence of an intense electric field. Ultra-high vacuum is required within the microscope's chamber (pressures smaller than 10^{-9} torr) to provide a long mean free path for the imaging electrons, and to retard the contamination of the specimen's surface.

The interpretation of some features of FIM images still remains controversial, especially the variations in image brightness from point to point.

As some of the least understood features have been observed in field-ion micrographs of nickel and its alloys, we decided to study nickel 20 at.% tungsten utilizing FIM in conjunction with FEM, hoping to

ascertain the causes for some of the observed image characteristics.

1.1. Field Emission

The emission of electrons from the surface of a condensed phase into another phase, usually vacuum under the action of a high electrostatic field (0.3 to 0.6 volts/Å) is called field emission.

Emission of electrons from a metal surface can be attained by supplying the electron with the energy necessary to overcome the potential barrier, that is the work function ϕ. When this energy is supplied by bombarding electrons we have secondary electron emission, when by photons we have photoelectric emission and when by phonons we have thermionic emission. In field emission, however, instead of overcoming the work function, the surface potential barrier is deformed by the field in such a way as to give electrons a higher probability of tunneling through.

For a triangular barrier of height ϕ and width ϕ/Fe (Fig. 1a), the tunneling probability has been found to be proportional to

$$\exp\left[-\left(\frac{2m}{h^2}\right)^{1/2} \frac{\phi^{3/2}}{Fe}\right]$$

for electrons at the Fermi level.

If the image potential or Schotky Effect is included, the triangular barrier is rounded up as in Fig. 1b and reduced by an amount $(e^3F)^{1/2}$.

Fowler and Nordheim[1] using this type of barrier calculated the current density of electrons produced by field emission, yielding the well known Fowler-Nordheim equation

$$J = 6.2\times10^{-6} \frac{(\mu/\phi)^{1/2}}{Ef+\phi} F^2 \exp\left(\frac{-6.8\times10^7 \phi^{3/2}a}{F}\right) \qquad (1)$$

where μ is the Fermi energy measured with respect to the bottom of the

conduction band, and is expressed, as ϕ in electron volts when F is expressed as electron volts/cm and J is amps/cm^2.

1.2. Field Emission Microscopy

A tip or sharply pointed cathode placed in a high vacuum pointing toward a zinc sulfide screen, produces an enlarged image of the emitting surface once a high potential between the cathode and the screen is established. The field at the surface of the cathode is related to the voltage V by using the expression

$$F = \frac{V}{kr} \tag{2}$$

where r is the mean radius of curvature of the emitter surface and k is a quasi constant that depends on the geometry of the electrodes ($k \simeq 5$).

As the image on the screen is a radial magnification of the emitter's surface, we can write the magnification attained as $R/\beta r$ where R is the emitter to screen distance, r is the emitter radius and β is a constant depending on the microscope's geometry ($\beta \simeq 1.5$).

The resolution δ of the field emission microscope in terms of distance on the emitter surface can be written as

$$\delta = 2.62\times10^{-4}\beta\, R^{1/2}\left(\frac{1.16}{\beta V^{1/2}} + \frac{1}{K\alpha\phi^{1/2}}\right)^{1/2} \tag{3}$$

where δ and R are in centimeters and V in volts[2] and α is a constant. The first term is the contribution of the transversal momenta and the second is the diffraction effect. For a crystal of 10^{-6} cm of radius, ϕ = 4.5 eV and F = 5×10^7 volts/cm the predicted resolution is of the order of 20 Å.

The origin of the brightness contrast in the field emission image

may be seen from the Fowler-Nordheim equation (Eq. 1). As the emitted electron current depends exponentially on $\phi^{3/2}/F$ then slight variations of work function and local field will be displayed in the image.

Variations of F reflect changes on the effective local radius of curvature (Eq. 2) and consists of relatively large-scale variations caused by the overall shape of the emitter and shorter range variations due to the topography of the surface. However, the dominant variable determining the contrast in the field emission image is the work function which changes with crystallographic orientation, composition and adsorbed impurities.

Summing up, the technique of field-emission microscopy permits the observation of small variations in the work function and local curvature of the specimens with magnifications of $\sim 10^{+5}$ and resolution of ~20 Å.

This technique has been applied in adsorption phenomena, work function measurements and diffusion phenomena, etc.

It has seldom been employed for the study of alloys, and in no case, known to this author, has it been employed to study nickel tungsten alloys.

1.3. Field Ionization

Field ionization is the ionization of a free atom by tunneling the electron through the deformed potential barrier (due to a strong external electric field). The field utilized in field ionization is much higher than that of field emission (2 to 5 volts/Å).

A high applied field deforms the potential surface of a positively charged anode in such a way that it permits the ionization of a free gas atom if the electron tunnels through from its ground state in the mother

atom into the metal surface as we can see in Fig. 1c. When the atom is near the surface, the atom becomes polarized and the effect of the proximity of its charge on the surface potential barrier further reduces the width by image forces.

The barrier penetration probability for the tunneling electron may be found by the W.K.B. approximation, yielding

$$D = \exp\left[-\left(\frac{8m}{h^2}\right)^{1/2} \int_{X_2}^{X_1} (V-E)^{1/2}\, dx\right] \tag{4}$$

where X_2-X_1 is the width of the potential barrier, m is the electron mass and E is the total energy.

The frequency of ionization is given by

$$f = \nu D \tag{5}$$

where ν is the frequency with which the electron hits the potential barrier as estimated from Bohr's atomic model.

The radius of curvature affects the local field as we saw in the expression $F = V/Kr$. Then the areas of larger radius of curvature will appear darker in the field ionization picture than those of smaller radius of curvature.

In general, the ion current produced by the imaging gas as it is ionized near the surface of the specimen depends on the amount of gas atoms available at the tip and the number of atoms being either ionized or diffused away from the tip's area.

Considering that all the atoms that arrive at the tip are ionized the ionic current is given by

$$i = \alpha S q \tag{6}$$

where α is a semiconstant depending on the number of the diffused ions, q is the ionic charge and S is the supply function given explicitly by

$$S = \sigma_{eff} P(2\pi KT)^{-1/2} \tag{7}$$

where $P(dynes/cm^2)$ is the gas pressure, and σ_{eff} is the effective cross section of the tip which differs from the geometric cross section σ_g by the factor $(1 - 2V(F)/3KT)$ where V(F) is the potential of a particle in the field F.

Thus the ion current can be written as

$$i = \alpha \left[1 - \frac{2V(F)}{3KT} \right] \sigma_g P(2\pi KT)^{-1/2} \tag{8a}$$

If we take into account that some of the atoms bounce on the tip and then instead of being ionized diffuse down the shank of the specimen, the ion current must be expressed as

$$i = 2\pi r_t^{\,2} x_c q C_t \frac{KiKd}{Ki+Kd}$$
$$x_c = \frac{I-\phi}{cF} \tag{8b}$$

where x_c is the critical approach at which an atom can be ionized. I is the ionization potential, ϕ is the work function and F is the applied field.

$$Ki = \left(\frac{KT}{2\alpha_p}\right)^{1/2} \frac{r}{T(I-\phi)} \exp \frac{\left(-2(I-\phi)\alpha_p F_o\right)}{\gamma \varepsilon KT}$$

$$Kd = \frac{(2KT)^{3/2}}{m^{1/2}\alpha_p F^2 r}$$

and

α_p = ionization probability, T = period spent by the atom, within ionization range, m = mass of the gas atom, r = radius of curvature.(3)

1.4. Field Ion Microscopy

In the field ion microscope the specimen is positively charged and gas is allowed at low pressure into the instrument's chamber. The image is formed on the fluorescent screen by the positive gas ions produced near the specimen's surface, when electrons from the gas atoms tunnel into the specimen. The magnification of the field ionization microscope is also a radial.

The field ionization microscope has a resolution of the order of an atomic diameter because of the larger de Broglie wavelength of gas ions, compared to that for electrons.

The minimum resolvable distance in the field ion microscope is given by:

$$\delta = 4r\beta(KT/Ve)^{1/2} \qquad (9)$$

where r is the tip radius, $\beta \approx 1.5$ (depends on geometry), V is the voltage (V=KrF) and T is the absolute temperature.(4)

For helium at -20°K the resolution attained is 3 Å for emitters of 1000 Å in diameter and V = 10^4 volts.

1.5. Field Evaporation and High Temperature Flashing

The last stage in the preparation of the FIM - FEM specimen requires attaining an almost perfectly hemispherical emitting surface, free of impurities and protruding atoms. This can be accomplished either by field evaporation or by heat flashing.

1.5.1. Field Evaporation

This technique is based on lowering the activation energy[5] required to evaporate an ion from the surface of a metal, by applying a high electric field.

The field required to evaporate surface atoms from kink sites on the metal surface depends on the sublimation energy λ, the ionization potential I_n and the work function ϕ of the plane containing the evaporating atom. This has been expressed, as:

$$F = (en)^{-3} [\lambda + \sum_n I_n - n\phi]^2 \qquad (10)$$

where n is the number of electrons depleted from the atom.

For a given applied voltage V the field F will be different for different sites of the specimen depending on the local work function and also on the local radius of curvature (Eq. 2).

The evaporation rate Ke, is an Arrhenius type of relation

$$Ke = \nu \exp[-Q/KT] \qquad (11)$$

$$Q = [\lambda + \Sigma I_n - n\phi_0] - (n^3 e^3 F0^{1/2} \qquad (12)$$

where ν is a frequency factor and Q is the activation energy for field evaporation. Q is, to a first approximation, temperature independent.

Thus, the evaporation rate depends exponentially on the work function and the field. A large work function will produce an increase of the exponential factor and a preferential field evaporation of the high work function area. Also a large local field, as produced by a protruding atom (a kink atom or an impurity) will produce preferential field evaporation of these atoms.

The field evaporation end form of the specimen will then present a smooth, almost spherical surface, topped by small regions of different radius of curvature. These local differences of radius of curvature produce differences of brightness in the field ionization photomicrographs.

1.5.2. Heat Flashing

The method of heat flashing consists of heating the tip electrically in vacuum to the point where contaminants decompose or evaporate. By this method alone it is hard to clean metals with melting temperature lower than 1300°K.

Heating at certain temperatures causes surface diffusion yielding a spherical bulb at the tip of the emitter and if heating is continued it produces blunting to a point where field ionization is no longer possible. Surface diffusion depends on the energy H_f necessary to produce mobile adhesion atoms and surface vacancies and the activation energy H_a to move the atom or vacancy on the surface. These energies depend on the atomic packing, thus they change from one surface orientation to another.

It is expected that formation of adhesion atoms on close-packed planes requires a larger energy H_f than on loosely packed planes. However, it should be easier to move an atom on the relatively smooth surface of a close-packed plane compared to on the rough surface of a high index plane.

These two factors account for a slight buildup of material on the tip's surface in certain crystallographic directions upon heating of the crystal up to temperatures where surface diffusion is possible.

The end form of a "buildup" tip will have accumulated surface atoms

at the low work function (low index) planes and a depletion of atoms at the high work function areas of the tip. Thus buildup accentuates the dark areas (high work function areas) of the emission micrographs. A more severe buildup can be attained if flashing is done with the high electric field on.

1.6. Image Interpretation of Field Ion Micrographs

Field ion micrographs of pure metals and alloys usually present regions of different brightness. The most outstanding features that are commonly observed are zone line decoration, symmetric regional image brightness, brightness contrast within the same crystallographic plane and dark zone or dark band symmetrical patterns.

The following is a brief description of these features and the explanations that have been published up to now.

1.6.1. Zone Line Decorations

Zone line decorations are rows of single atoms and groups of atoms that are substantially brighter than the rest of the atoms observed in the FIM. They occur along zone lines like the (110) - (100) sector of the tungsten micrographs (Fig. 2a).

These zone lines have been explained by Müller[6] as isolated atoms sitting at metastable surface sites, however, Tong and Gilman[7] showed that the outstanding bright spots could be resolved into groups of three or four (triads and tetrads) on metastable positions.

1.6.2. Regional Brightness

Symmetric regional image brightnesses are brighter regions observed at a specific crystallographic orientation, bright regions could be accounted for by varying local radii of curvature due to preferential field evaporation.[8]

The brightest region of tungsten is the {111} region and the darkest is the {110} region (see Fig. 2). Also the radius of curvature in the {110} region is several times larger than that of the {111} region. This dependence of brightness on radius of curvature can be better understood from Eq. 8. The larger r is, the smaller the ion current I will be.

1.6.3. Zone Brightness Contrasts

Brightness variations along certain zones are specially obvious in tantalum molybdenum and platinum. These sharp contrasts around regions that are assumed to have the same radius of curvature have been explained by Moore and Brandon[9] by taking into account the changes in the atomic environment of the imaged atoms. They suggested that atoms with more than a critical number of first and second nearest neighbors do not appear in the field ion image, and that the bond geometry of more distant neighbors can be correlated with overall variations of intensity in different areas of the stereographic triangle formed by {100}, {110} and {111} poles as vertices.

Müller and Tsong[10] explained the same variations with an electron orbital model for field ionization. It is possible that the explanations of Müller and Moore can be correlated, as both are based on the nearest neighbor's effect on the imaging atoms.

1.6.4. Dark Zone Patterns

Dark zones have been observed in micrographs of different metals under some imaging conditions. These are symmetrical dark bands stretching from one major crystallographic pole to another on the image. In some ways they are similar to the previously described brightness

variation. These are very conspicuous effects in nickel alloys (Ni_4Mo) and have received ad-hoc explanations by different authors. The effect of dark zone regions was observed initially in nickel-molybdenum, by LeFevre, Grengu and Ralph,[11] who observed a dark band pattern in the field ion micrographs of Ni_4Mo. They pointed out that these bands do not go through domain boundaries and did not seem to be symmetric with respect to the image. They tend to pass through fundamental planes and by-pass the major superlattice planes. They explained that the superlattice planes contain Ni and W layers alternately, while the fundamental planes are mixed. Thus, as W tends to image preferentially, the fundamental planes will tend to look darker. This appears to be the origin of these dark zones.

Newman and LeFevre[12] also worked with Ni_4Mo and observed not only the dark zone pattern joining the major fundamental planes, but a secondary zone pattern, of thinner bands, which joined the superlattice planes. They attributed the dark zone pattern to the shape of the Fermi surface (following Nakamura and Müller). They considered that regions where the Fermi level approaches the Brillouin zone boundary correspond to directions in K space for which there is a reduced number of available energy states, thus a smaller probability of electrons tunneling in. The ionization probability of helium atoms is then smaller in these regions.

Using the shape of the Fermi surface of Ni, they concluded that as it necks up toward the (111) direction (if we assume it is spherical elsewhere) that would explain the darker bands in Ni_4Mo around the (111) planes. However, Newman and Hren[13] working with ordered and disordered

forms Ni_4Mo did not find the zone pattern at liquid helium temperature. No paper considering band structure in the disordered Ni_4Mo is known to the author.

The explanations for zone decorations, symmetric regional image brightness and brightness contrasts within the same crystallographic plane have been fairly well accepted by field ion microscopists. However, there does not seem to be agreement in the origin of dark band formations as they appear in nickel and some of its alloys. The dark band patterns have been variously explained by different authors. There does not seem to be enough information to conclusively determine which of the possible explanations is correct.

The present work was undertaken to further substantiate the existence of dark bands and to clarify the conditions necessary for their appearance in an FIM image.

2. THE METALLURGY OF Ni_4W

Alloying nickel and tungsten has been important to industry since it provides one of the earliest methods of making tungsten ductile. It is also important as a basis for acid resistant alloys. The most recent nickel-tungsten phase diagram, due to Ellinger and Sykes,[14] is reproduced in Fig. 3. From the melting point of nickel (at 1726 ± 4°C) the liquidus curve rises to a maximum (1505°C) at 35% W, and then falls to 1495°C, the eutectic temperature. The alloy of eutectic composition contains 45% W. It was believed, by earlier investigators, that the maximum in the liquidous was associated with a compound, Ni_6W capable of existing in two dimorphic states, the β state, stable above 900°C and the α state stable only at lower temperatures. At the present time it is believed that Ni_6W does not exist and that the solid phase (α) separating from the liquid in hypoeutectic alloys, is a solid solution of tungsten in nickel. The limiting solubility at the eutectic temperature is at about 40% W decreasing up to 38% at 970°C and to 32% at 800°C.

On cooling to 970°C, a peritectoid reaction occurs between α and the tungsten-rich solid solution γ to give an intermediate phase, β, containing 43.93 percent W.[15] Due to the marked change in solid solubility with falling temperatures, alloys containing 32 to 45% W exhibit age hardening. Aging occurs very slowly at temperatures of the order of 600°C, but relatively quickly at about 900°C. The resistance of nickel to corrosion by sulphuric acid is greatly increased by alloying with tungsten, an alloy containing 18% tungsten showing a minimum rate of solution, less than one fortieth the rate for pure nickel.

The tensile strength of nickel falls to a minimum at 25% tungsten,

and then increases. By suitable heat treatment, a Brinell hardness of the order of 490 can be obtained in alloys containing 32-45 %W. Also, there is a linear increase in the electrical resistivity up to 25%W. The nickel tungsten alloys might find industrial applications in the fabrication of jet turbines and any other instrumentation requiring high strength and high temperature metals.

As we said before, the only phase formed peritectoidally, according to Ellinger and Sykes, is Ni_4W (43.93% W) which is the object of our study. Ni_4W has a certain range of homogeneity that can be estimated to 2 weight percent (3 at. %) at 900°C and it has been suggested to have a low tungsten boundary at 17.6 % W or even lower, below 850°C.

After quenching the Ni_4W alloy anneal two phases will be present. The tungsten rich (γ) phase appears as small inclusions evenly distributed in the nickel rich (α) matrix.[16] Thus, there is a much higher probability of imaging the α phase in FIM and whenever we mention the as-quenched alloy we are actually refering to the α phase with 38% W content.

This phase has the same structure as nickel, it is fcc with the same structure as nickel, it is fcc with a lattice parameter a_{fcc} = 3.6248. A slight contraction occurs upon ordering (below 970° ± 10°C) and the new phase body centered tetragonal structure.

The unit cell of the β phase contains 8 Ni atoms and 2 tungsten atoms. The parameters for the bct lattice are a = 5.730 and c = 3.553, c/a = 0.620. This makes the space group c^5_{4n} - I_4/m. There are six possible crystallographic orientations of a given ordered domain with respect to the original fcc matrix. Two of these orientations are shown

in Figs. 4a and b. The unit cell is rotated by an angle $\theta = 18.4°$, with respect to the fcc unit cell.

From the geometry it can be seen that the crystal can be constructed by alternating tungsten layers with four nickel layers parallel to the superlattice planes (Fig. 5a). The fundamental planes [as (211) which corresponds to (111) in the disordered structure] are formed of layers of intermixed nickel and tungsten atoms (see Fig. 5b).

3. EXPERIMENTAL PROCEDURE

3.1. Preparation of the Alloy

The nickel-tungsten alloy was prepared from an ingot of pure Ni (99,9%) and GE 0.218 W wires, melted in an arc furnace with an excess of 1 atomic percent Ni to make up for evaporation. The product of the melting was then swaged and homogenized at 1300°C in vacuum (10^{-7} torr) for 90 hrs, three consecutive times. The alloy so produced was chemically tested and found to be 20 at. % W and 80 at. % Ni. Further swaging and annealing was required until wires of 0.011 in. diameter were obtained.

3.2. Heat Treatment

These wires were then annealed in a helium atmosphere at 1300 ± 10°C for 144 hours and quenched into water. Two batches of wires were separated; those as-quenched and the second batch, annealed at 850° for 168 hours in an argon atmosphere.

3.3. Preparation of the Specimen

The actual tips for the field-ion microscope were made of pieces of the polycrystalline wires spot welded to a holder or mount. (See description of the equipment in Appendix I.) The wires were then electropolished until a diameter of 500 to 1000 Å was attained at the tip. The following two electropolishing procedures were used:

Procedure A

A polishing solution suggested by Müller[17] for tantalum composed of: 4 parts 48% hydrofluoric acid, 2 parts concentrated sulfuric acid, 2 parts concentrated phosphoric acid, 1 part concentrated glacial acetic acid was used. This mixture was diluted with 75% in volume of pure water.

For the ordered material an initial potential of 32 volts dc was used until thinning was noticed. Then the tips were finished by slow electropolishing at 18 V giving short electric pulses of 0.1 sec or less until the desired tip diameter was obtained. If voltages lower than 18 volts were used, a nonconductive film was deposited on the tip. This film could be removed by etching in 1N NaOH at 5 volts dc. Several metals were used as cathodes but tungsten, tantalum and stainless steel 304 were preferred.

For the as quenched material, the initial voltage was about 12 volts. The final shaping was obtained with short pulses of 0.10 and 0.05 sec at a potential between 2 and 5 volts dc.

Procedure B

Electropolishing in 25% hydrochloric acid solution in water, using 10 volts ac for the initial thinning and 2 volts ac for the final shaping for both ordered and disordered tips. However after each immersion in the etching solution, it was found necessary to "clean" the tips from nonconductive films by electropolishing in 1N NaOH, with a short (1/5 sec) pulse at the same etching voltage. The NaOH does not attack the tip material appreciably, but long exposures to it will cause the formation of an oxide film which is removable by electropolishing with the HCl solution. The final shape of the tip was always ascertained with an optical microscope at ×500 magnification. Most of the tips had preferential etching along the shaft and care had to be put into the final shaping. Tips that had a relatively thick shaft and a thin-end point were preferred as they seemed to better withstand the high strains produced during the field evaporation process.

The tips after electropolishing, were washed in water and alcohol and mounted on the glass multiple-tip cryostat. The final preparation of the imaging surface was done through field evaporation in helium gas or high temperature flashing in vacuum (see Sec. 1.5.).

3.4. Temperature Control

To produce the required range of temperatures for the experiment, a glass-metal cryostat was used and the specimens were cooled using low temperature helium gas transferred from a standard liquid helium container. A resistor in the helium container, electrically heated by a controlled ac source, provided the vapor pressure to force the liquid helium to transfer.

Currents of 1.2 ma were found sufficient to maintain enough flow of liquid helium toward the cold finger to maintain temperatures of 10°K at the tip holders (as ascertained with a thermocouple). Currents of 0.5 ma were enough for temperatures around the liquid nitrogen range. During operation these current readings and the characteristics of the image itself (resolution of single atoms) were taken as rough indicators for the specimen temperature.

3.5. The Equipment

The equipment utilized in this experiment was a versatile metal field-ion-field-emission microscope constructed from a basic design by Dr. H. C. Tong and adapted by the author for these experiments (Fig. 6).

Pressures as low as 1.5×10^{-10} torr could easily be obtained and maintained in the apparatus, thus allowing for field emission observations after 6 hrs baking at 120°C and 10 hrs pumping time. A glass-metal cryostat, that allowed four specimens to be viewed during

each run, and also permitted high temperature flashing of the specimens was utilized (Fig. 7). A gas supply of hydrogen, neon and helium was readily available in the apparatus. Also devices to measure electron currents (Faraday cage) and charge to mass ratios (atom probe) were incorporated. These last two devices were not utilized in these experiments.

4. EXPERIMENTAL RESULTS

In this chapter the information pertaining to the dark band pattern in Ni_4W obtained with the field-ion microscope is presented. The results of the field emission mode observations is left as part of the discussion for dark-band formation.

4.1. The As-quenched Alloy

The field ionization photographs of the as-quenched specimens, in general, had well developed low index poles (Fig. 8), which were visible as dark circles sometimes surrounded by incomplete rings but in general a disordered appearance.

The specimens showed a preferred {111} orientation toward the center of the FIM image or in some cases a {100} orientation was observed. These orientations are to be expected due to the swaging and annealing process used to produce the wires.

At liquid nitrogen temperature or above, violent field evaporation was present even when a relatively small voltage was applied. Also at this temperature, wide dark symmetrical bands were visible. A micrograph with a [111] tip orientation showing the dark band pattern can be seen in Figs. 9 and 10. At liquid helium temperature field evaporation was still present at the best imaging voltage, making it difficult to obtain a stable image.

Specimens oriented toward the (100) pole showed, in addition to the dark zone pattern already mentioned, zones of less darkness emerging from the (100) pole and directed toward the (111) poles (see Fig. 11). (Compare with the stereographic projection in Fig. 12).

Subsequent field evaporation and observation of the specimens at liquid helium temperatures, showed clearly the low index poles but not the dark band pattern (Fig. 13). Thus, the dark band pattern is observed only at temperatures around liquid nitrogen boiling point (~78°K) when the image is very unstable and the tip is continuously field evaporating. The pattern disappears at temperatures around liquid helium boiling point (~4°K).

When the temperatures were reduced from liquid nitrogen to liquid helium temperatures maintaining the same potential the bands that were clearly visible at liquid nitrogen temperatures almost disappeared at liquid helium temperatures. However as field evaporation almost stops around liquid helium temperatures, it was not possible to definitely ascertain whether the bands disappeared due to cooling or due to cessation of field evaporation at lower temperatures.

The Ni_4W dark band pattern differs from that observed in Ni_4Mo, basically in the presence of only three large dark zones radiating from the (111) pole instead of the six dark zones present in Ni_4Mo.

4.2. The β Phase

The samples that were produced from the material thoroughly annealed at 850°C showed a high degree of ordering in the liquid helium temperature FIM pattern (Fig. 14). At temperatures close to the liquid nitrogen boiling point, violent field evaporation was produced and thin dark bands were often observed emerging from most of the low index planes (Fig. 15) at lower temperatures, (Liquid He boiling point) in tips that were not fully developed. These tips were observed at liquid helium temperatures after field evaporation at slightly higher temperatures.

It was noticed that some of the dark bands were decorated by strings of very brightly imaging atoms along its borders.

Due to the incomplete development of the tips presenting the dark bands, it is hard to say if the bands follow any particular symmetry.

4.3. Summary of the Results

Two different phenomena observed in Ni_4W field ion micrographs were described above as dark band patterns:

a) Dark zones in the as-quenched alloy

b) Dark bands in the β phase.

The first phenomenon was shown to depend on the imaging temperature and may be dependent on the temperature of field evaporation. The second phenomenon was only observed in ordered tips at liquid helium temperature and relatively high gas pressure.

5. DISCUSSION OF RESULTS

5.1. Dark Band Zones in the As-quenched Alloy

We have shown that the dark band patterns that appear in as-quenched Ni_4W are heavily dependent on temperature. Müller and Tsong[18] show micrographs of Ni at 78°K and 21°K, where the first one presents an almost identical dark band pattern to that of Ni_4Mo but the second micrograph does not show any apparent bands. This temperature dependence is also apparent in the micrographs of Ni_4Mo of LeFevre et al., where only micrographs taken at temperatures around liquid nitrogen show the dark bands. There are not published pictures of dark bands known to the author taken at temperatures below 20°K. Therefore, the explanation for the bands given by Newman and LeFevre (Sec. 1.6.4., page), using the Fermi energy model can only be possible if it could be shown that there is a dependence of the Fermi energies on small temperature changes.

It is known that the Brillouin zones and the Fermi energy, change with phase transformations.[19] That is, if a new periodicity is introduced a new Brillouin boundary appears and the Fermi levels themselves are perturbed. However, there are no changes in structure due to changes in temperature ($\Delta T \approx 50°K$) far from the crystallographic phase transition temperature (970°C).

It seems clear then, that the temperature dependence of the FIM pattern observed cannot be explained by the Newman-LeFevre model alone. However, Fermi surfaces might have, as they suggest, some bearing on the observed pattern. LeFevre's model (Sec. 1.6.4., page 11) considering that mixed planes (fundamental planes) will image darker due to preferential imaging of W on the superlattice planes, does not hold in

the disordered alloy, because all the planes are mixed planes, yet there is preferential imaging of certain planes. Moreover, it cannot explain the bands present in pure nickel micrographs. Either Müller's or Moore's explanations of the brightness variations across certain zones, might apply to the conspicuous dark zone pattern in nickel. But it is hard to visualize from their formulation how the temperature dependence of the observed patterns can be accounted for.

The observations described in the previous chapter seem to suggest that the dark band pattern observed is actually due to the topology of the specimen, which depends on field evaporation. The variation with temperature of the FIM pattern might depend either on the temperature of the last field evaporation or the temperature at which the image is observed. A model explaining the dark band effect based on the observations, will be introduced in the following section.

5.2. A Model for the Dark Zone Pattern in the As-quenched Alloy

5.2.1. Geometrical Argument for the Existence of Dark Zones

A consideration of the topographic characteristics of the field evaporation end form of the specimen and the imaging characteristics of the same at different temperatures, provides a model to explain the dark zone patterns in Ni_4W as well as those in other materials.

In section 1.5.1. (page 8) it was stated that the field evaporation end form of a specimen is a quasi-hemispherical surface topped by small regions of different radius of curvature.

These local differences of curvature produce differences in brightness due to the radial dependence of the local external field affecting the potential barrier for field ionization.

Areas of higher work function will be preferentially evaporated (Eq. 11 and 12) until a large enough local radius of curvature is attained so as to reduce the local field and stop the preferential evaporation process (Eq. 12).

In order to visualize the geometry of the field evaporation end form of a specimen, three dimensional models have been constructed with balls representing atoms. These models are limited to small radial sizes and therefore the number of crystallographic planes that can be present. They do not allow the representation of high index planes.

Computer simulations of spherical tips have provided a more powerful method for image interpretation as they allow different imaging criteria to be tried out for comparison with the actual micrographs. Among the criteria tried are different thickness of the outer shell within which the imaging atoms lie, dependence of imaging on coordination number, electron energy distribution, non-spherical topography,[24] etc.

Moore and Ranganathan[20] have used computer simulated images from crystals of varying radii of curvature to show that the thickness of the shell of atoms contributing to the image increases for smaller crystal radii. They also arrived at a visibility criterion that for a plane to be recognized in the image at least three parallel close-packed rows should be visible.

The prominence of the planes is determined by the interplanar distances even if interference of the planes is allowed for. They listed the planes to be expected on selected zones of spheres of various radii. Such a list was compiled with the help of the computational procedure

mentioned above.

Following a similar procedure Washburn and Tong[21] produced a computer model of a fcc spherical crystal using the lattice parameters of Ni_4W (Fig. 16). An observation of the image produced by the model shows fewer but larger planes developed in the (111) - (110) sector than in the (111) - (100) sector and a much larger density of smaller planes developed in any other direction. A developed plane center differs greatly in radius of curvature from the hemispherical surface, thus it will show in the field ionization micrograph as a darker area. If planes overlap along a line [as in the (111) - (110) sector], the whole region will appear as a darker zone than the surrounding areas.

To represent a random solid solution of 20 at. % W in Ni where only 20% of the atoms were allowed to appear in Fig. 17. This is equivalent to assuming that only W atoms will appear. That is, 80% of the atoms that would have appeared in a normal fcc FIM pattern were randomly subtracted from the image.

This is the actual imaging condition of the as-quenched alloy. Even in this case it is easily noticed that the density of imaged atoms in the (111) - (110) sector is lower than that of the (100) - (111) sector, and substantially lower than any other area.

The density of spots in the (111) - (110) and (111) - (100) sectors of the computer image was ascertained by counting spots in an area of 1 cm width. This was compared with counts in other areas outside these sectors. These results are compared with similar counts made on an actual field ion micrograph of an as-quenched specimen at 4.5°K and 78°K (Figs. 9 and 18).

From Table I, it is clear that a smaller density of spots appears in the computer simulated image in the (111) - (110) sector, and that a similar effect contributes to the dark zone pattern observed in as-quenched alloys at 78°K. However, there is not a significant difference between the density of spots in the (111) - (100) sector and other areas.

This geometrical argument for the existence of dark zones, does not provide a complete explanation because the darker zones appearing in the simulation are not as conspicuous as those in the micrographs at 78°K.

5.2.2. The Possible Contribution of Preferential Field Evaporation to the Dark Zone Pattern.

As we indicated before, the areas of large work function should be preferentially field evaporated as can be expressed by the evaporation rate (Eq. 11 and 12).

$$Kc = \nu \exp\left[(-\lambda + \Sigma I_n - n\phi_o) - (ne)^3 F^{3/2}\right] \frac{1}{KT}$$

thus if the planes along the dark zone pattern have a relatively larger work function than the surroundings, an area of even larger average radius of curvature could be produced by preferential field evaporation accentuating the image contrast between the (111) - (110) sectors and secondly the (111) - (100) sectors from the surroundings.

It is therefore of interest to ascertain if there is such a work function difference. A simple qualitative method to observe differences of work function is field emission microscopy as explained in section 1.2 (page 3). The brightness contrasts in field emission micrographs depend primarily on work function differences rather than on small differences of local radius of curvature.

A low work function area will appear lighter than a high work function area in FEM. If the (111) - (110) sectors have an appreciably higher work function than the other sectors of the tip, they should appear as dark bands in the field emission micrographs.

A series of experiments to ascertain the work function differences in Ni_4W were undertaken and also previous results in pure nickel field emission micrographs were considered.

Gomer[22] presented a field emission micrograph of nickel where the work function along the (001) - (111) sector of the [011] zone line is apparently much larger than in the surrounding areas. In the field emission micrograph of Ni_4W with a (111) orientation (Fig. 19) there are also dark areas along these zones suggesting higher work functions. The second highest work function area from Gomer's emission micrograph of Ni coincides with the sector between the (111) and (001) planes.

In the FEM of Ni_4W these sectors also have shown relatively high ϕ and in the FIM of Ni_4W with (100) orientation there are dark zones of less prominence emanating from the (100) pole (Fig. 11).

Therefore, the areas of high work function, depicted by field emission micrography of Ni_4W, coincide with the observed dark zone patterns in field ion micrographs. Thus it seems likely that dark bands in FIM patterns are previously discussed, enhanced by preferential field evaporation of the high work function areas.

5.2.3. The Temperature Dependence of the Dark Zone Pattern

Tsong and Müller[23] measured FIM image brightness for various gases under different imaging conditions and converted the image brightness into ion currents on a relative scale. The ion current was

shown to decrease rapidly with increasing imaging temperature. The ration $I(T_1)/I(T_2)$ at two different temperatures depends on field strength as is shown in Fig. 17. Apparently, at a very low field the ion current is essentially determined by the exponential factors in Eq. 8b, and therefore the ion current increases steeply with the fields and decreases very rapidly with the elevation of temperature.

A difference of local field intensity at the surface of a specimen will produce a larger image brightness change at 78°K than at 21°K, as can be seen from the curves in Fig. 20 .

The (111) - (110) sectors in the field evaporation end form of Ni_4W appears as a dark zone in FIM and we have shown that it corresponds to regions that are relatively flatter than the rest of the tip, therefore, they have a lower effective field than the rest of the tip. Thus, from the curve of Fig. 20a , the change in ion current occurring in the (111) - (110) sector upon cooling from 78°K to 21°K would be larger than the change in ion current occurring in the other areas of the tip.

The magnitude of this effect can be illustrated by making an estimate of the possible local variation in field. Suppose the (111) - (110) sector has an average field intensity of 3.6 V/Å at a given voltage, and the sector (111) - (113) has a field intensity of 5.0 V/Å at the same voltage then the variation of ion current from 78°K to 21°K is:

Sector	I(21°K)/I(78°K)
(111) - (110) (dark zones)	12.5
(111) - (211) (bright areas)	7.5

Then the variation of current with temperature for the dark areas is 67% larger than the current variation for the bright areas. Therefore reasonable field differences will produce, significant temperature dependence of the contrast between low field and high field areas.

The large change in ion current for the low field (dark zone) region and the smaller change in the high field (bright) region will produce an image of even brightness at low temperature. Therefore, the dark band regions tend to disappear from the field ionization pictures at low temperatures.

The difference of the dark-band pattern in Ni_4W and those observed in Ni_4Mo and Ni, can also be explained by this model. The field emission patterns of Ni and probably that of Ni_4Mo, show almost the same darkness on the sectors of the (100) zones between (111) and (110) planes and the sectors projecting from the (111) planes to the (100) planes. However, in Ni_4W only the sector between (111) and (110) plane shows substantially darker.

This is the same as saying that the (111) - (100) and (111) - (110) sectors of Ni should present more or less the same preferential field evaporation while the sectors (100) - (111) will present lower field evaporation rate than the (110) - (111). This is apparent in the field ion micrographs and field emission micrographs of Figs. 13, 14 and 20, 21.

5.3. The Ordered Alloy

The results of FIM in the ordered alloy showed that no dark band pattern was clearly visible in the micrographs of fully developed specimens at normal imaging conditions, but dark bands were visible in specimens not fully developed at pressures higher than the best imaging pressure.

These bands seem to be the site of relatively flat areas of few atomic distances in width and few atomic distances in depth. If we make a model of a flat area of these dimensions we notice that the bordering atoms will be in a protruding position, therefore, according to Smolukowsky's model, these atoms will be more electropositive and behave as better ionization sites than the neighboring atoms. This will explain the shiny rows decorating the sides of the band. This effect is not apparent in the as-quenched alloy probably due to the broadening of the band.

The rest of the atoms in the band are also darker than the atoms outside of the band and this is due to the flattening of the region due to preferential field evaporation as in the as-quenched alloy.

The appearance of these bands at 4.2°K as well as at higher temperatures can be expected as the image intensity differences do change with temperature as before, but the well defined borders of the band, due to the ordered position of the imaging W atoms show clearly the areas at low temperature.

6. SUMMARY AND CONCLUSIONS

The field emission micrographs of the Ni_4W as-quenched from 1300°C showed a dark zone pattern when the specimen was observed at temperatures around the liquid nitrogen boiling point (78°K). The bands seemed to depart from the {111} poles and oriented toward the {110} poles. A second, less dark pattern was observed extending from the {100} poles toward the {111} poles. The dark band patterns as a whole disappear upon cooling of the specimen to around liquid helium temperatures (4.2°K).

The field ionization micrographs of the alloy annealed at 850°C for 187 hours, showed a dark zone pattern at liquid nitrogen temperatures that persisted at liquid helium temperatures if the imaging gas pressure was sufficiently high. The dark band pattern was explained using a topographic model based on preferential field evaporation at dark band regions of the specimen due to a higher work function at these regions.

Previous explanations of the dark band pattern in pure nickel and in Ni_4Mo, fail to account for the temperature dependence and other characteristics. The use of FEM in conjunction with FIM has proven effective in making it possible to discard some of the previous hypotheses and in ascertaining the work function as the primary cause behind the dark band formation.

ACKNOWLEDGMENTS

The author wishes to express his deep appreciation and gratitude to Prof. Jack Washburn and Dr. Hua-Ching Tong for their advice and continuous support throughout the course of this investigation, and to Dr. Paul Okamoto for the fruitful discussions and helpful ideas during the early stages of this work. Special thanks are due the support personnel at the Glass and Mechanical Shops and the Technical Photography Department.

Thanks are also due to Mrs. Linda LeBorgne and Mrs. Shirley Ashley for their advice in the organization of the manuscript and the typing of it and to Mrs. Gloria Pelatowski for the art work.

This work was performed under the auspices of the U. S. Atomic Energy Commission through the Inorganic Materials Research Division of the Lawrence Radiation Laboratory, Berkeley.

REFERENCES

1. Gomer, Field Emission and Field Ionization, (Oxford University Press, London, 1961, p. 19.

2. Gomer, Field Emission and Field Ionization, (Oxford University Press, London, 1961), p. 42.

3. Gomer, Field Emission and Field Ionization, (Oxford University Press, London, 1961), p. 80.

4. Gomer, Field Emission and Field Ionization, (Oxford University Press, London, 1961), p. 95.

5. Müller, E. and Tsong, T. T., Field Ion Microscopy Principles and Applications, (Elsevier, New York, 1969), p. 58.

6. Müller, E. and Tsong, T. T., Field Ion Microscopy Principles and Applications, (Elsevier, New York, 1969), p. 203.

7. Tong, H. C. and Gilman, J. J., Structure of Anomalously Bright Atomic Groupings Seen in Field Ion Microscopy in The Structure and Chemistry of Solid Surfaces, G. Somorjai, Ed., Wiley and Sons (1962), p. 1 to 70.

8. Müller, E. and Tsong, T. T., Field Ion Microscopy Principles and Applications, (Elsevier, New York, 1969), p. 192.

9. Moore, A. J. and Brandon, D. G., The Effect of Bond Number on Atom Images in the Field Ion Microscope, Phil. Mag., 679-689 (1968).

10. Müller, E. and Tsong, T. T., Field Ion Microscopy Principles and Applications, (Elsevier, New York, 1969), p. 193-203.

11. LeFevre, B. G., Grenga, H. and Ralph B., Field Ion Images from Ordered Ni_4Mo, Phil. Mag. 18, 1127 (1968).

12. Newman, R. W. and LeFevre, B. G., On Contrast Variations in Field-Ion Images, Phil. Mag., 241-245 (1968).

13. Newman, R. W. and Hren, J. J., Field Ion Microscopy of Ni-Mo Alloys, Phil. Mag., 211-214 (1967).

14. Finley, H. E. and Wesley, P. S., The Nickel-Tungsten System in the Transactions of ASM, XXVIII, No. 3 (1940) 619-645.

15. Smithells, C. J., Tungsten, (Chemical Publishing Co. Inc., New York, New York, 1953).

16. Finley, H. E. and Wesley, P. S., The Nickel-Tungsten System in the Transactions of ASM, XXVIII, No. 3 (1940) 619-645.

17. Makamura, S. and Muller, E., Field Evaporation End Form of Tantalum, J. Appl. Phys. 36, (8) (1965).

18. Müller, E. and Tsong, T. T., Field Ion Microscopy Principles and Applications, (Elsevier, New York, 1969) p. 314.

19. Kittel, C., Introduction to Solid State Physics, (John Wiley & Sons, Inc., 1966); Nicholas, J. F., Effect of the Fermi Energy on the Stability of Superlattice, Proc. Phys. Soc. LXVI (3-A), 201-208 (1952).

20. Moore, A. J. W. and Ranganathan, S., Phil. Mag. 16, 723 (1967).

21. Tong, H. C. and Washburn, J., Private communication.

22. Gomer, Field Emission and Field Ionization, (Oxford University Press, London, 1961), pp. 35 and 45.

23. Müller, E. and Tsong, T. T., Field Ion Microscopy Principles and Applications, (Elsevier, New York, 1969), p. 38.

24. Ranganathan, S., Lyon, H. B. and Thomas, G., J. Appl. Phys., 38, 4957 (1967).

Table I. Density of spots (imaged atoms) in the field ion microscope and computer simulation pattern of as-quenched Ni_4W.

	Field Ion Micrograph	Computer Simulation
Sector	Density $\left(\frac{\text{spots}}{\text{cm}^2}\right)$	Density $\left(\frac{\text{spots}}{\text{cm}^2}\right)$
	$78°_K$	
(111) - (110)	5.0	3.54
(111) - (100)	30.0	7.05
Random areas	30.0	10.05

FIGURE CAPTIONS

Fig. 1. a. Triangular potential barrier for field emission used to calculate the tunneling probability.

b. Potential barrier including the image potential.

c. Potential barrier at the surface of a positively charged anode deformed in such a way as to permit the tunneling of an electron from a free gas atom impinging against the metal surfaces.

Fig. 2. Field ionization micrograph of tungsten:

a. Arrow shows the zone line decorations

b. Regional brightness in the {111} region.

Fig. 3. Phase diagram of Ni_4W after Ellinger and Sykes.

Fig. 4. a and b. Crystallographic orientations of a given order domain of the β phase of Ni_4W with respect to the α phase.

Fig. 5. a. Alternating tungsten layers with four nickel layers parallel to the superlattice planes.

b. Layers of intermixed nickel and tungsten atoms forming the fundamental (211) plane.

Fig. 6. Photographs of the field emission-field ion microscope.

Fig. 7. Diagramatic drawing of the field emission-field ion microscope;

1. Specimens (tips)
2. Cold finger (cryostat)
3. Glass window with quartz screen cover with a phosphorescent material.
4. High voltage connections. The other two connectors are at the sides of the microscope and are not shown in this drawing.

Fig. 8. FIM of as-quenched Ni_4W showing a disordered structure and a well developed (111) pole at the center.

Fig. 9. Micrograph of Ni_4W with a [111] tip orientation showing the dark band pattern.

Fig. 10. Stereographic projection of cm fcc crystal with the same orientation as Fig. 9 showing the bands.

Fig. 11. FIM with a [100] orientation showing the dark pattern directed from the [100] pole to the [111] poles.

Fig. 12. Stereographic projection of an fcc crystal with a [100] orientation, showing the dark bands mentioned in Fig. 10.

Fig. 13. FIM of the same tip of Fig. 11 after cooling to liquid helium temperature.

Fig. 14. FIM of Ni_4W β phase showing the highly ordered pattern with small imperfections.

Fig. 15. FIM of showing Ni_4W β phase dark bands in tips that are not fully developed.

Fig. 16. Computer simulation of a field ion micrograph of an fcc spherical crystal using the lattice parameters of Ni_4W.

Fig. 17. Computer simulation representing a random solid solution of 20 at. % W in Ni where only 20% of the atoms were allowed to appear.

Fig. 18. Field ion micrograph of as-quenched Ni_4W showing well developed planes and slightly lower density of imaging atoms in the {111} - {110} sectors. (Courtesy of Washburn and Tong).

Fig. 19. Field emission micrograph of as-quenched Ni_4W with a [111] orientation. Dark zones represent areas of higher work function.

Fig. 20. $I(Ti)/\pm(.T_2)$ versus field strength for helium imaging gas

a) $T_1 = 21°K$, $T_2 = 78°K$

b) $T_1 = 78°K$, $T_2 = 300°K$.

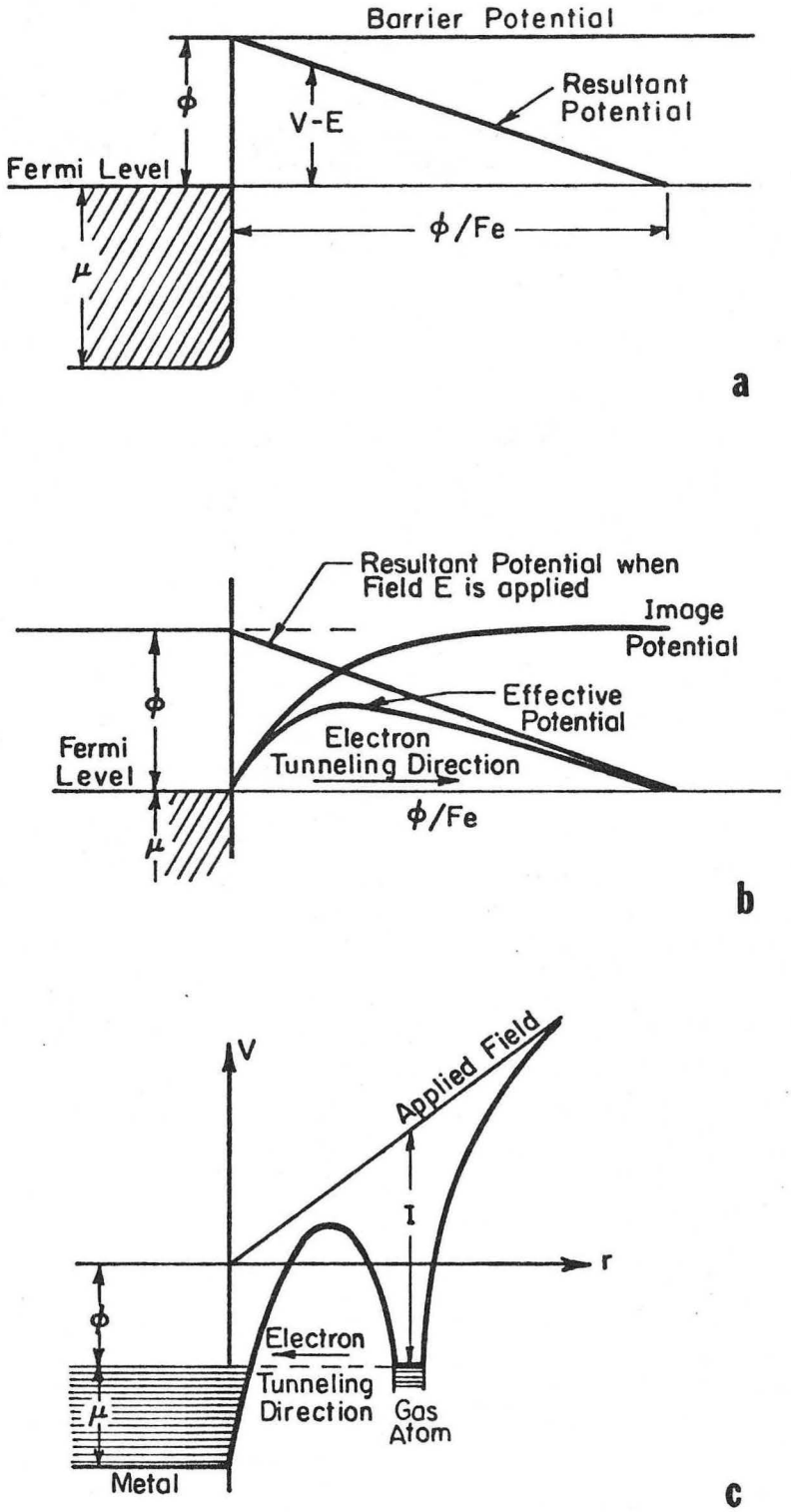

XBL 7012-7374

Fig. 1.

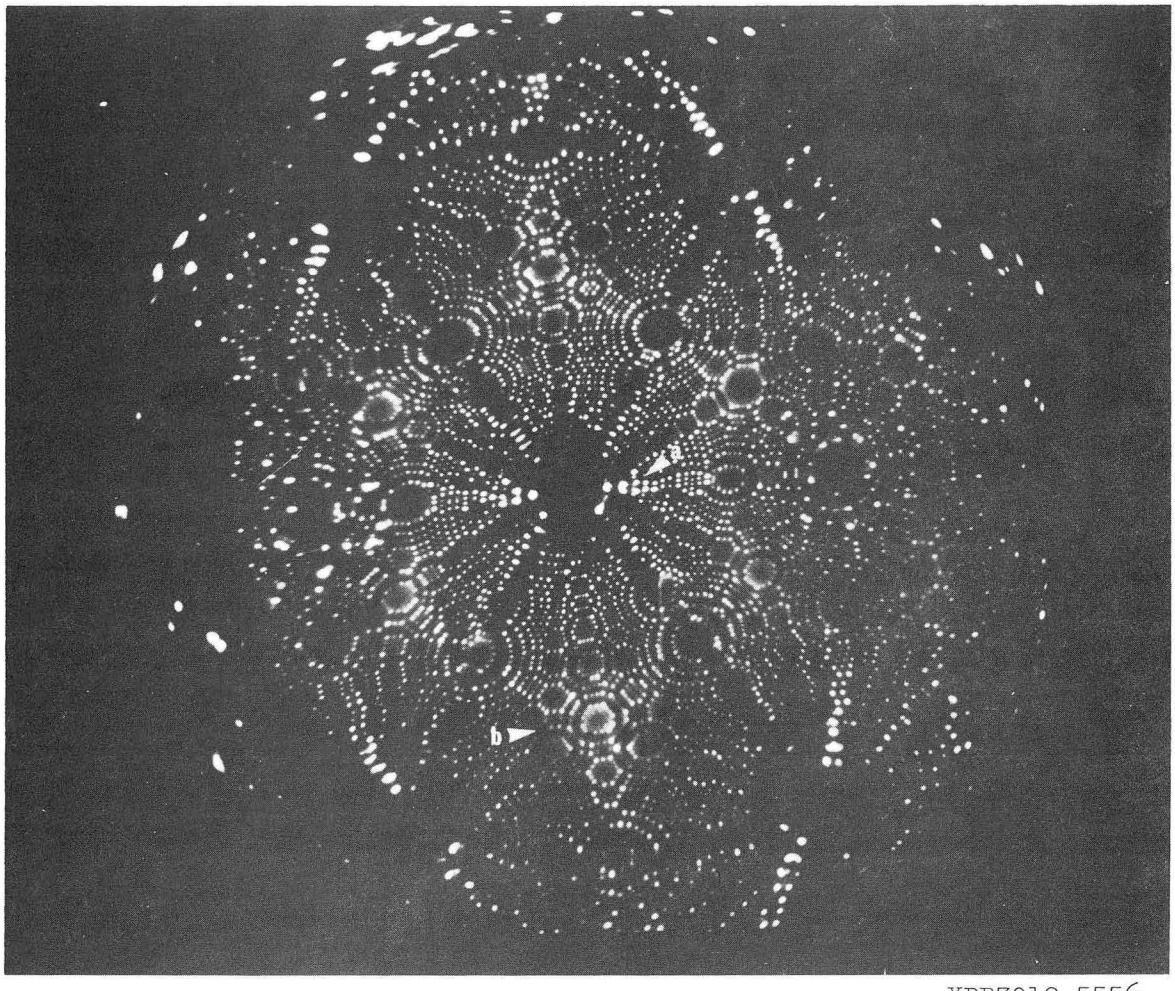

XBB7012-5556

Fig. 2.

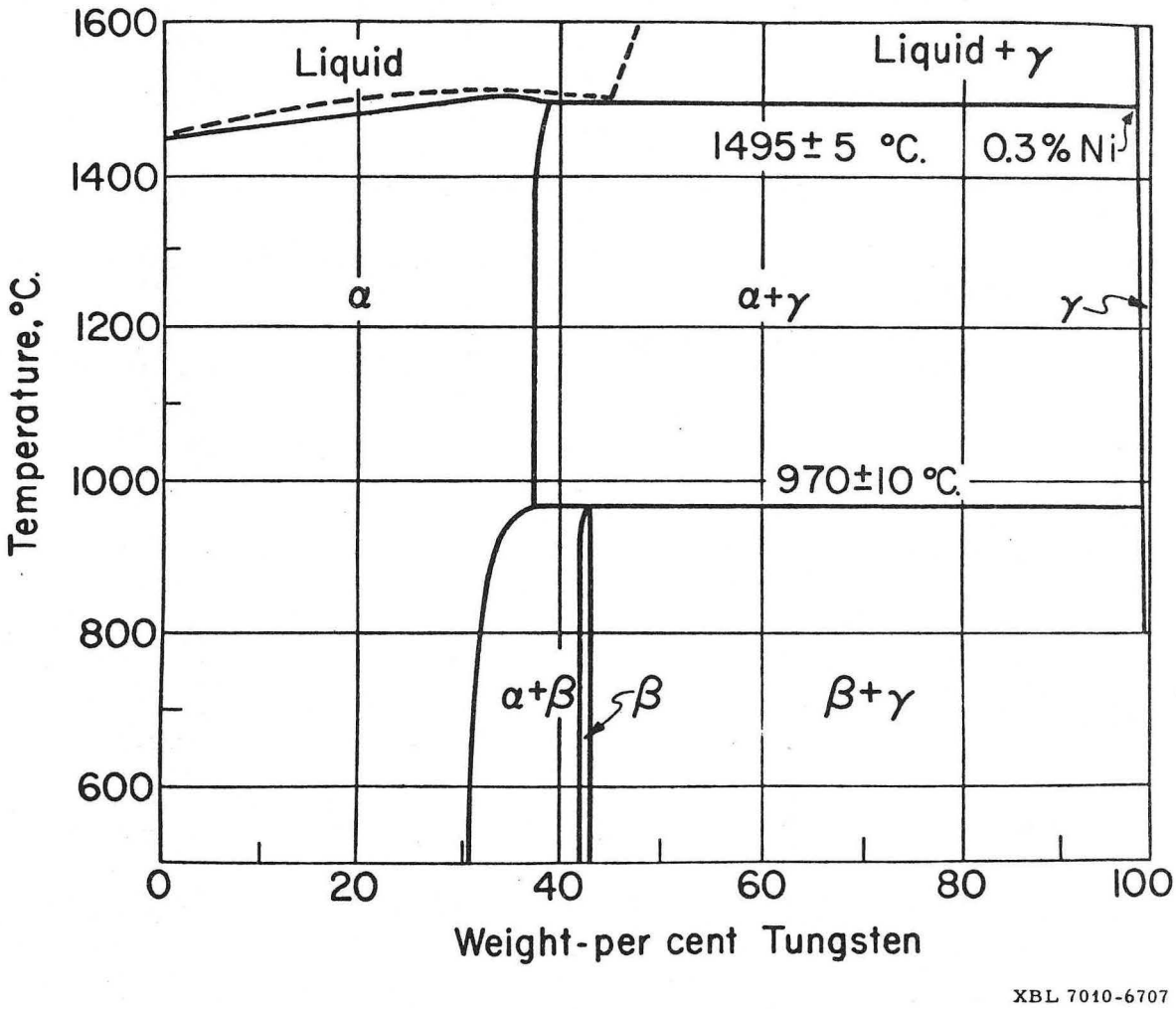
1600
1400
1200
1000
800
600
Temperature, °C.
Liquid
Liquid + γ
1495 ± 5 °C.
0.3% Ni
α
α+γ
γ
970±10 °C.
α+β
β
β+γ
0
20
40
60
80
100
Weight-per cent Tungsten
XBL 7010-6707

Fig. 3.

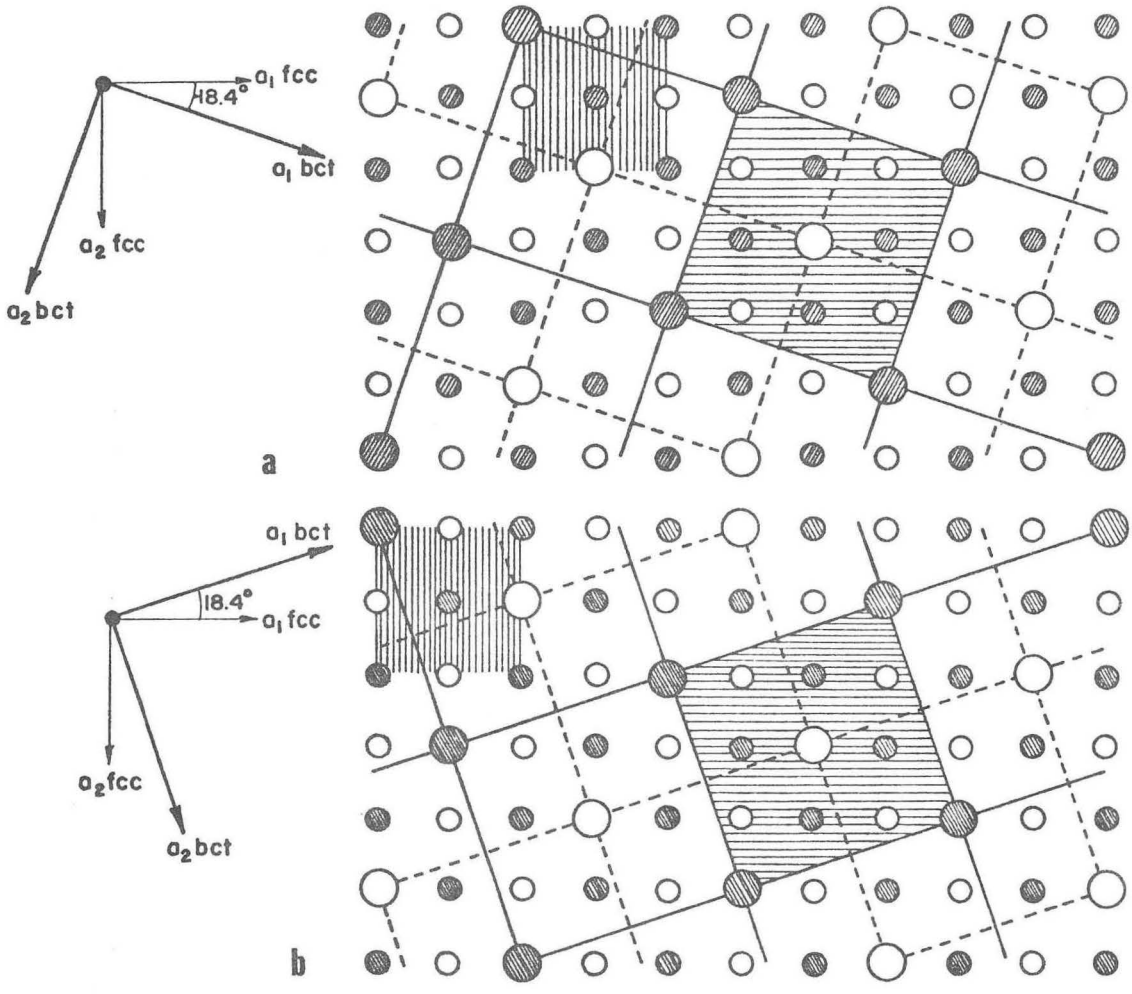
a1 fcc
18.4°
a1 bct
a2 fcc
a2 bct
a
a1 bct
18.4°
a1 fcc
a2 fcc
a2 bct
b
XBL 7012-7369

Fig. 4.

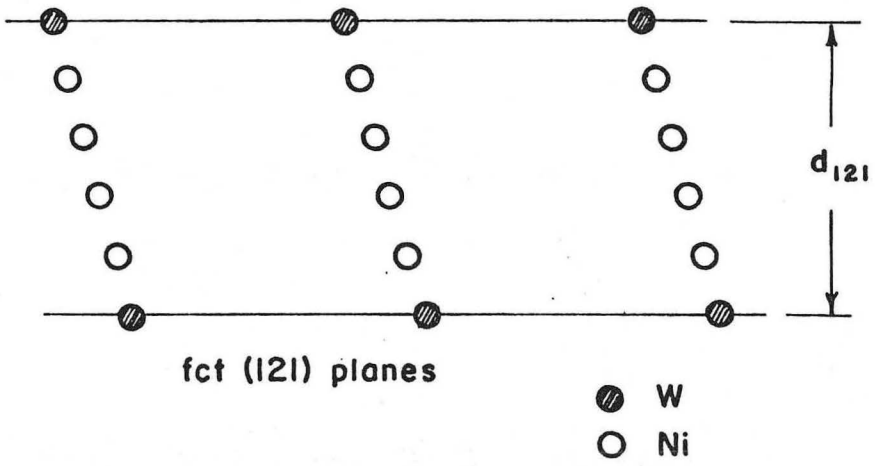

(a)

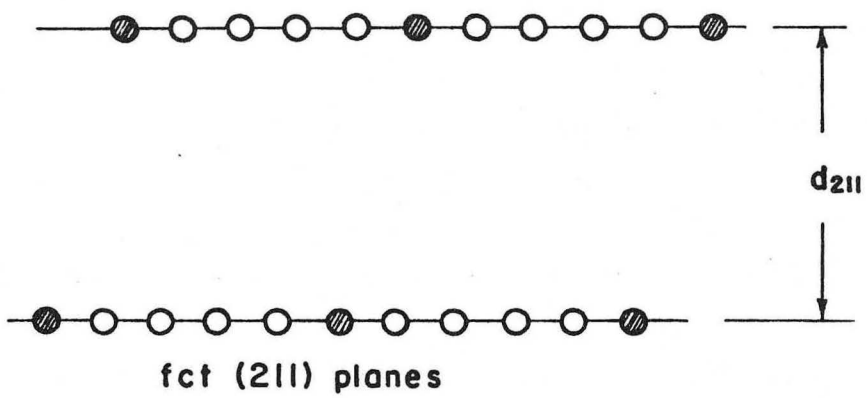

(b)

XBL 7012-7373

Fig. 5.

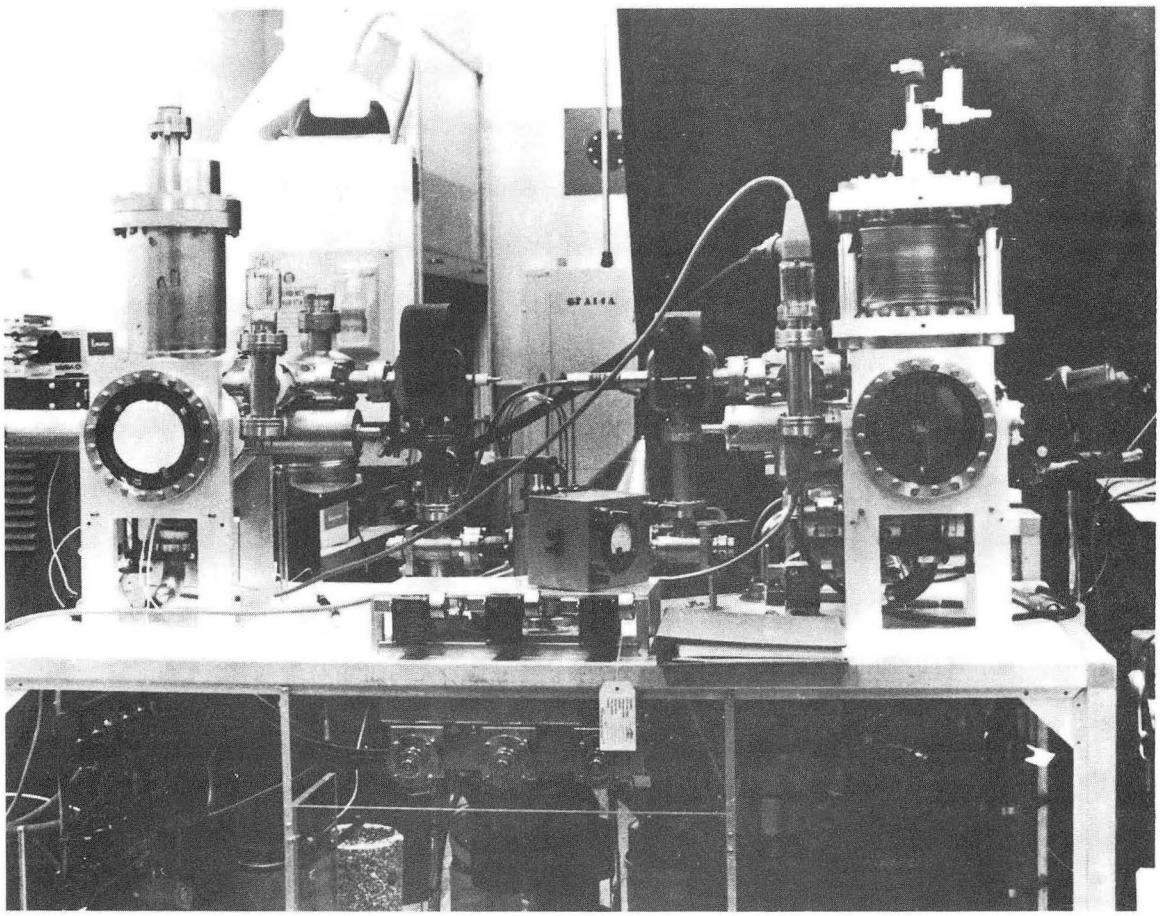

XBB7012-5557

Fig. 6.

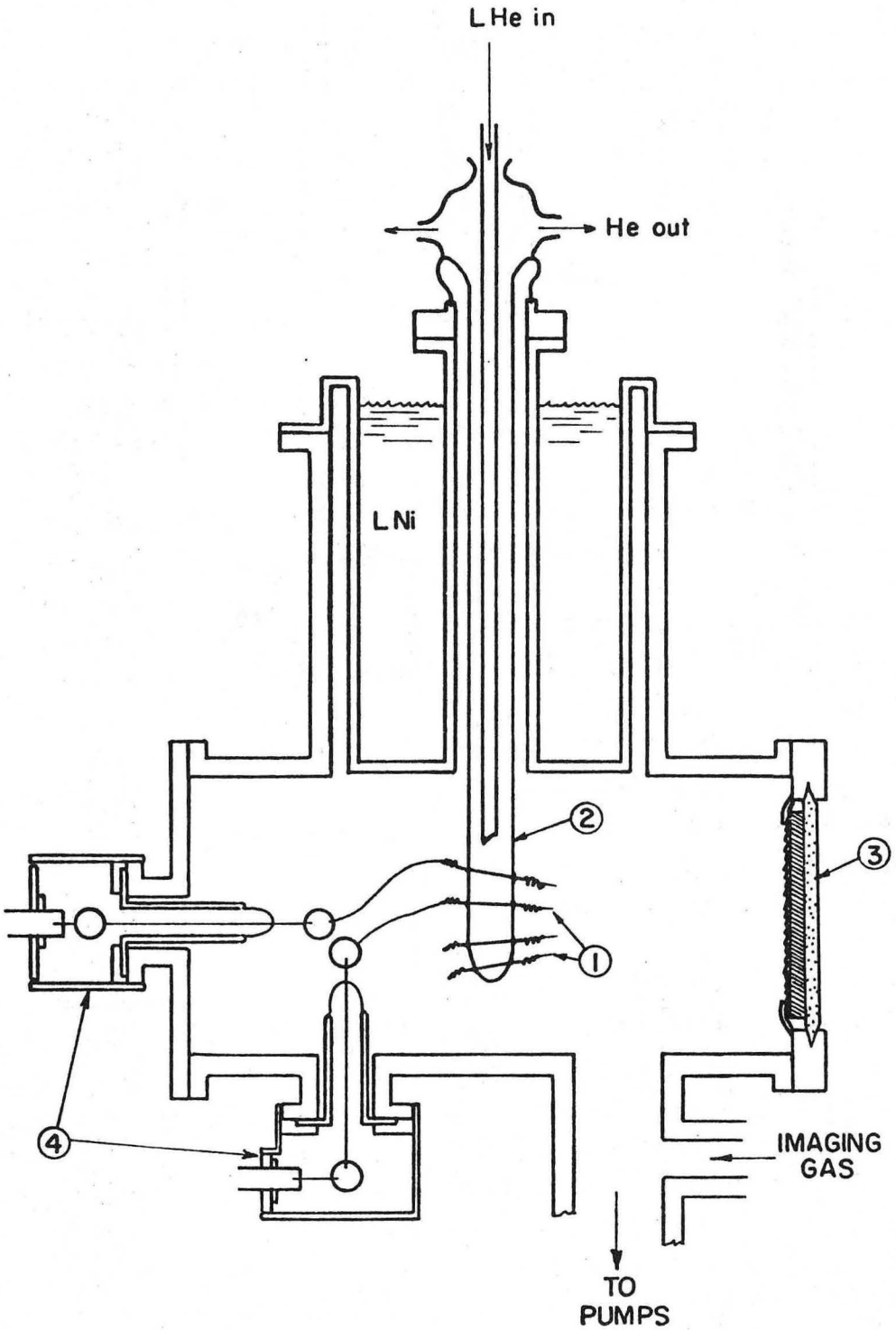

Fig. 7.

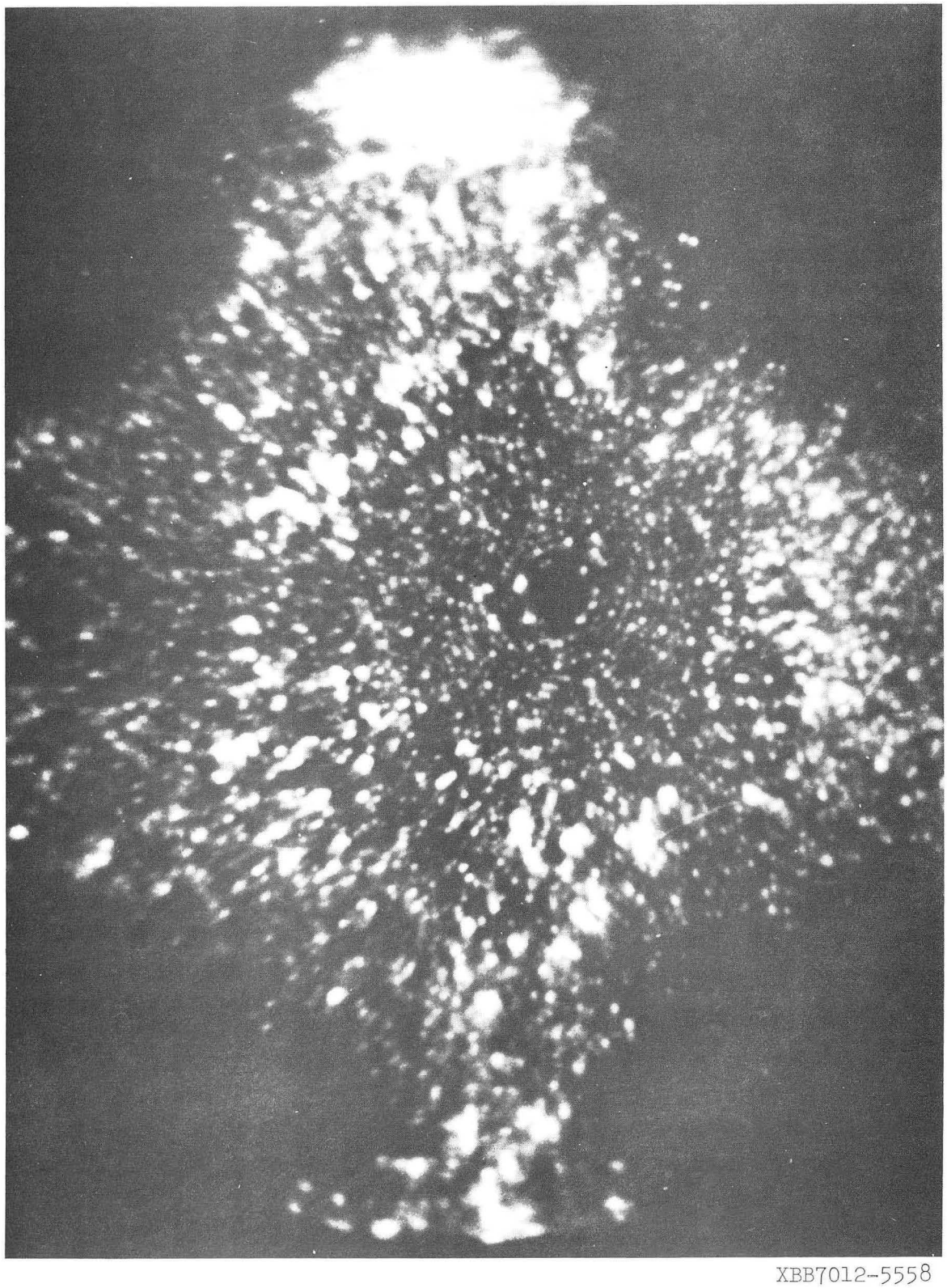

XBB7012-5558

Fig. 8.

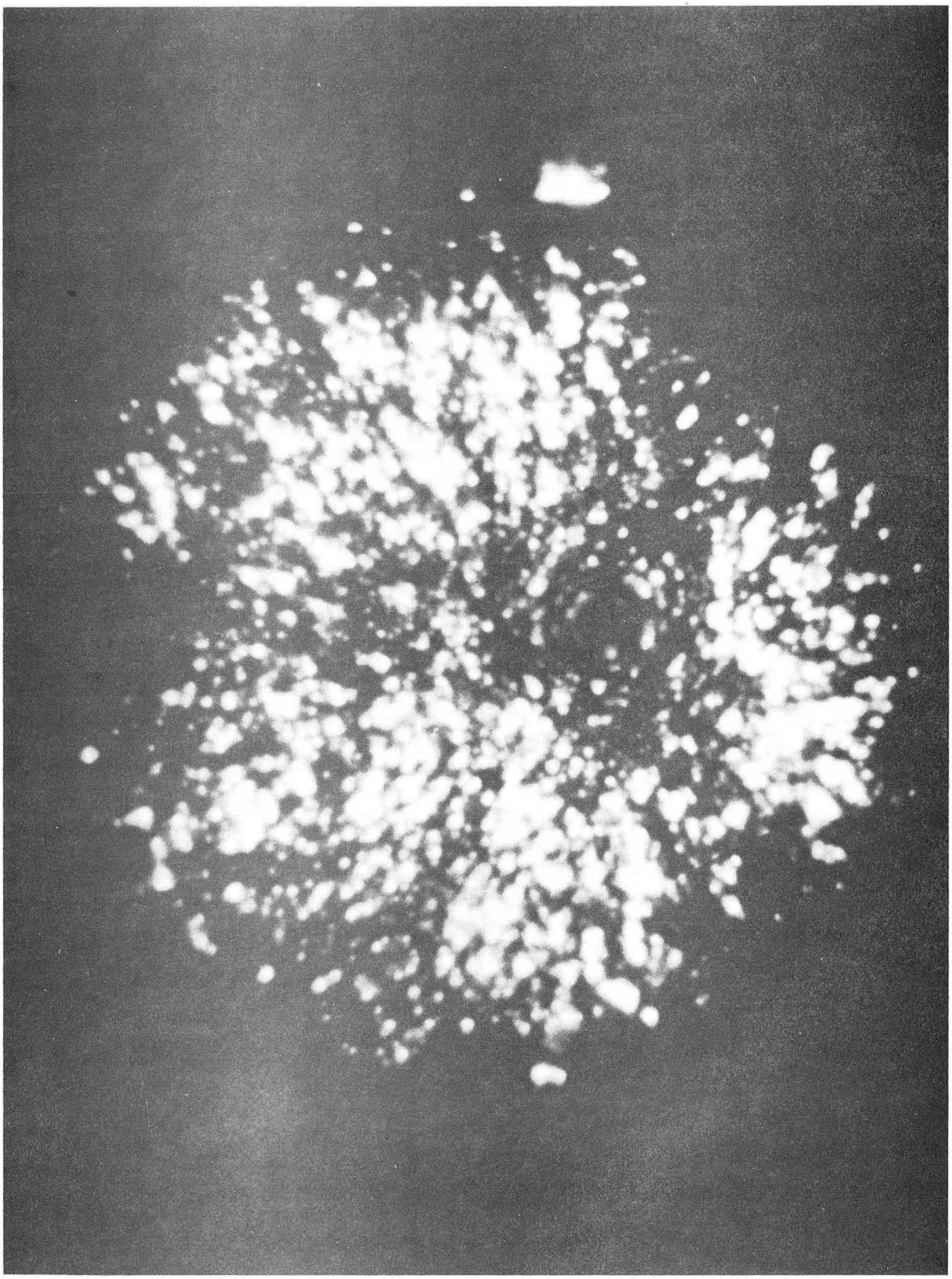

XBB7012-5559

Fig. 9.

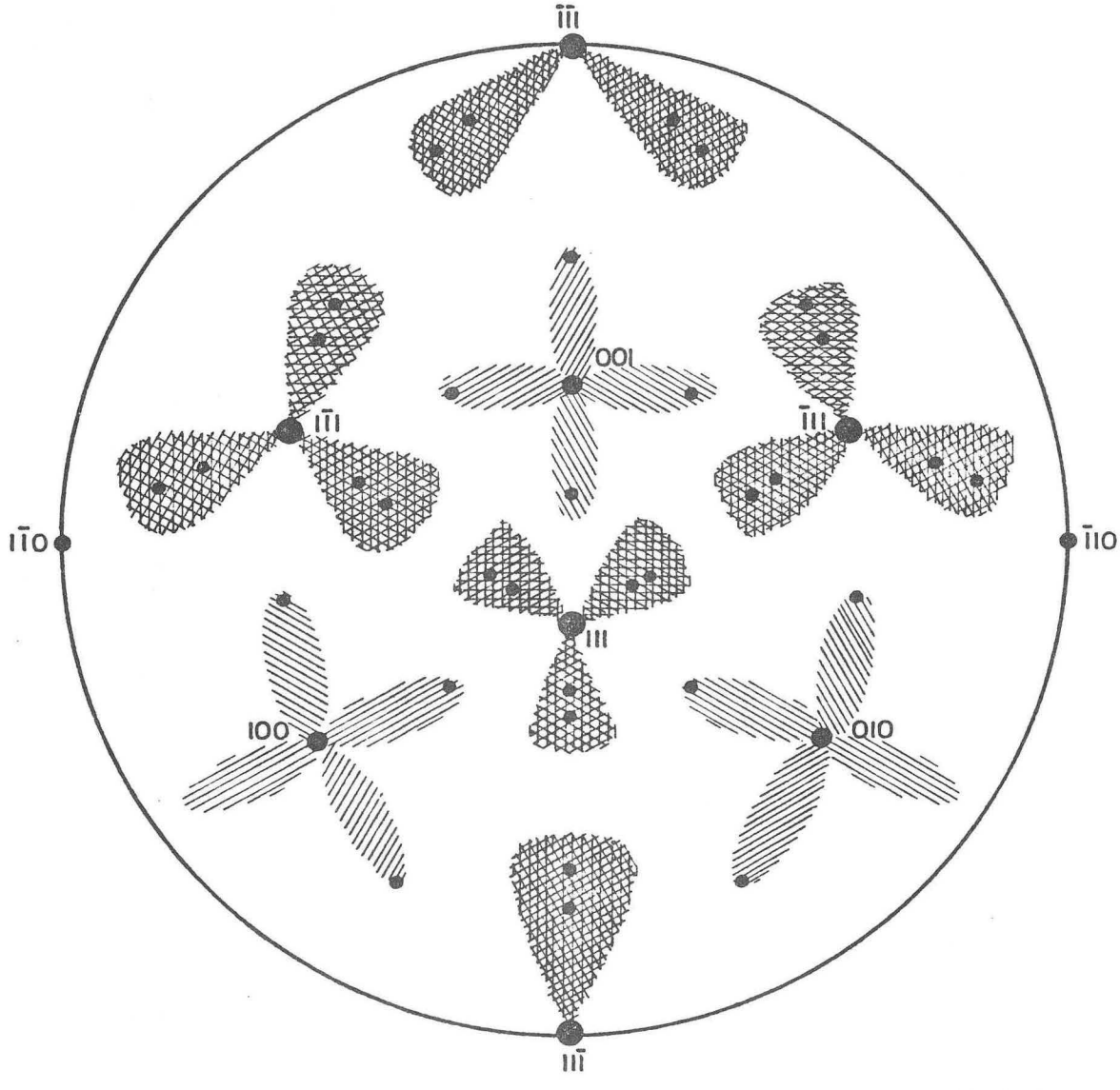

XBL 7012-7372

Fig. 10.

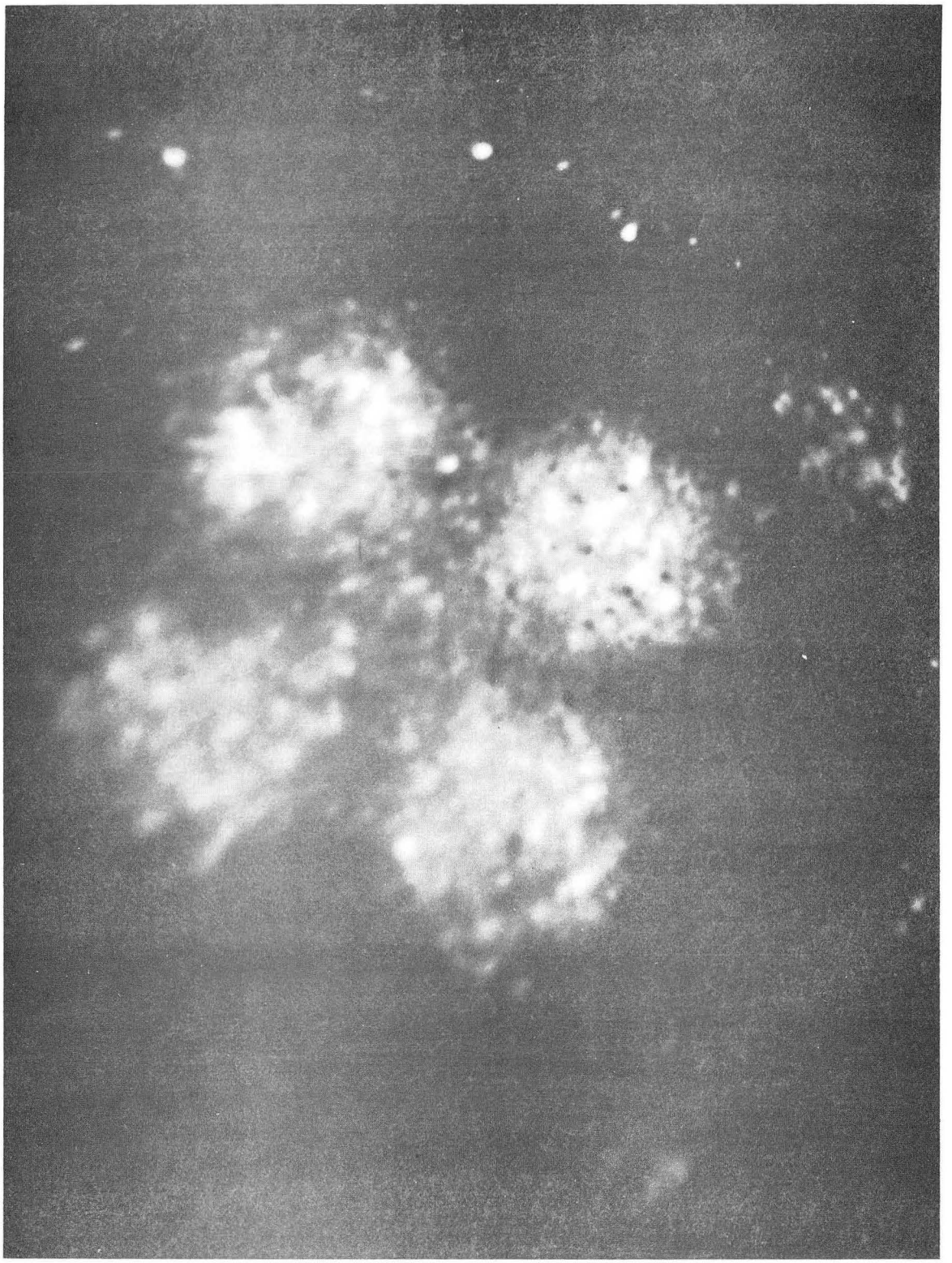

XBB7012-5560

Fig. 11.

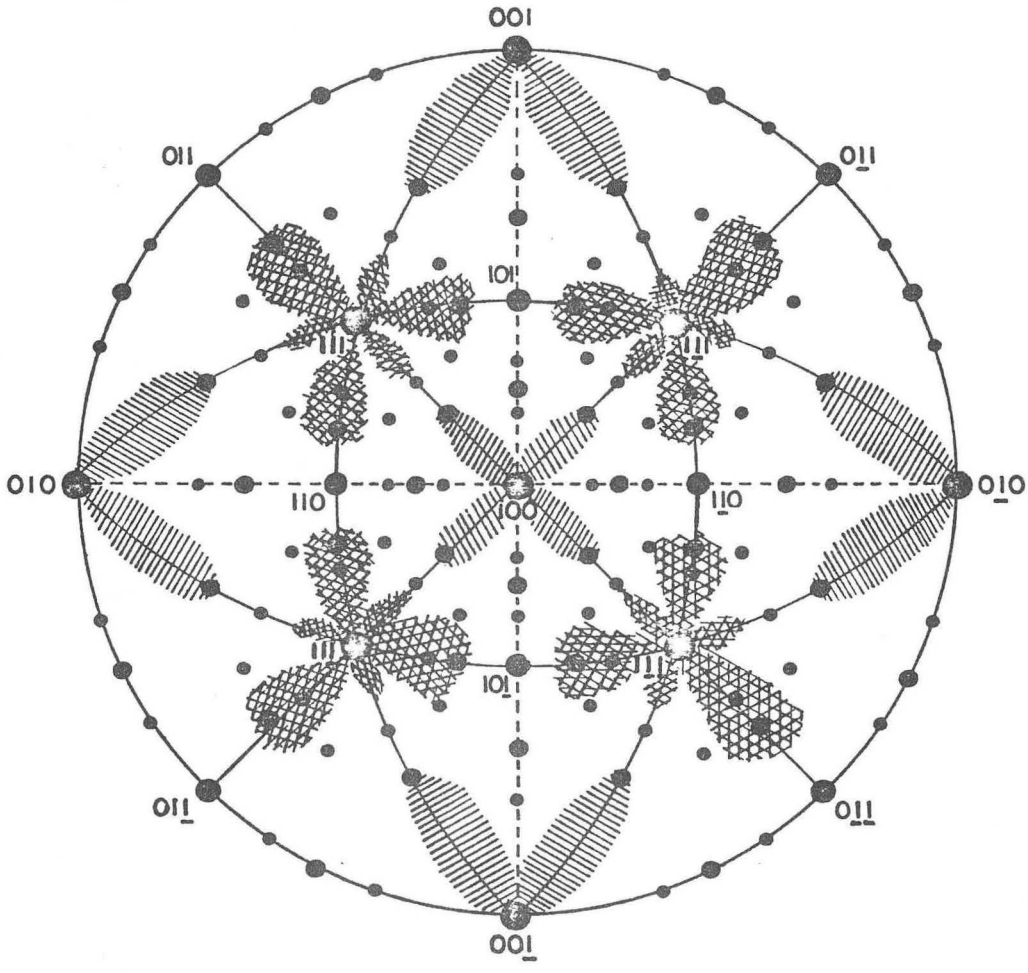

XBL 7012-7371

Fig. 12.

XBB7012-5561

Fig. 13.

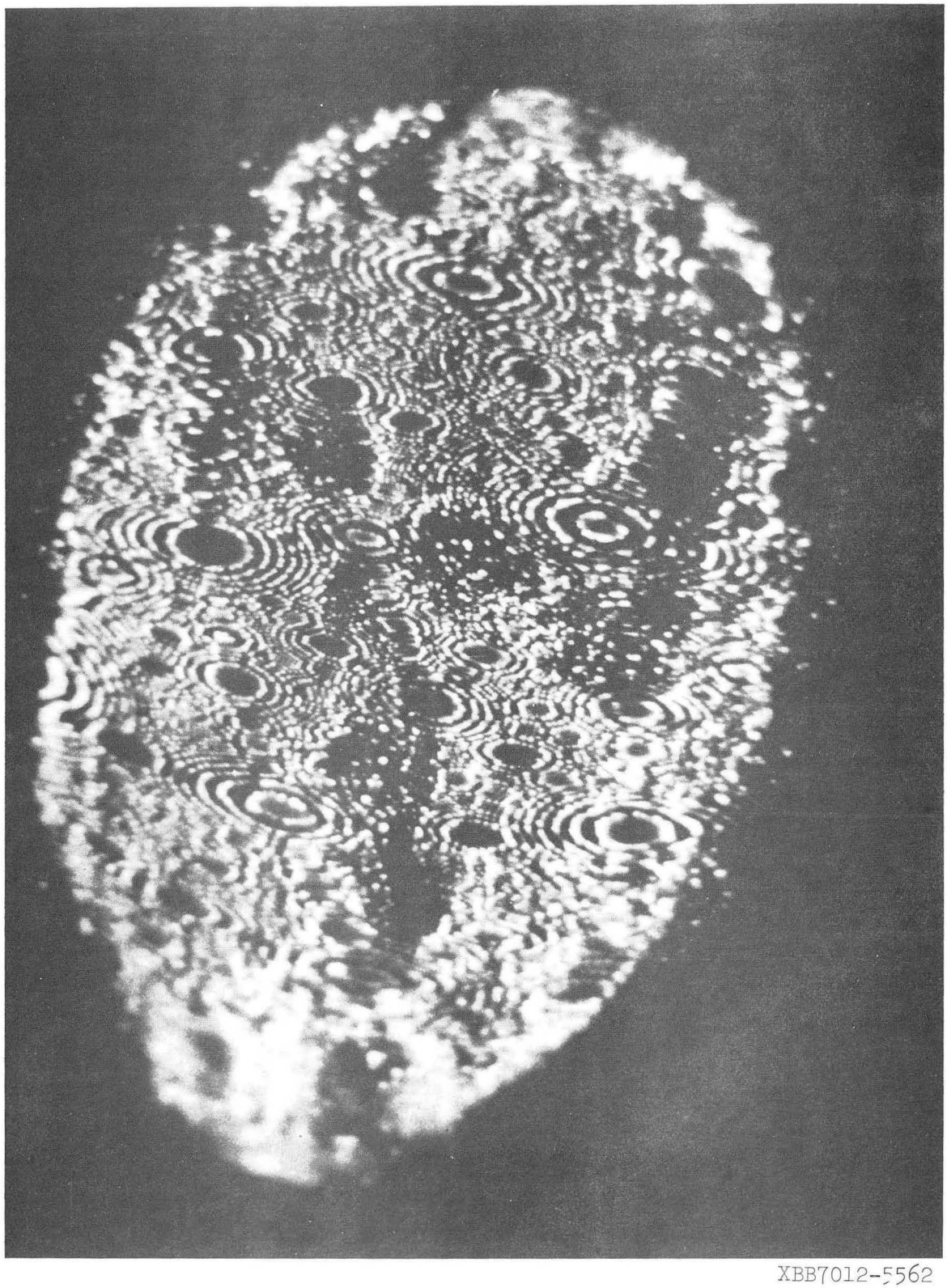

XBB7012-5562

Fig. 14.

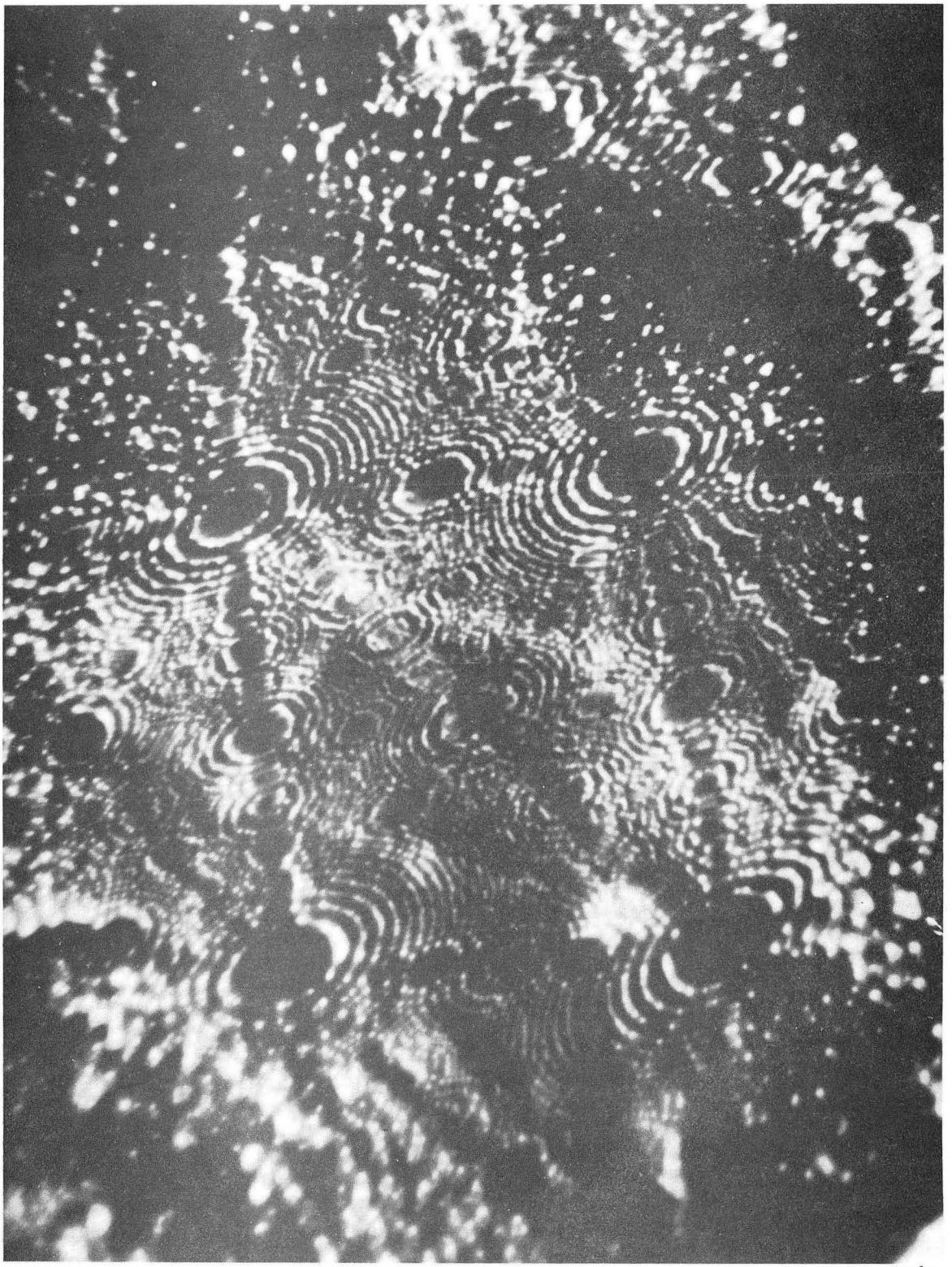

XBB7012-5563

Fig. 15.

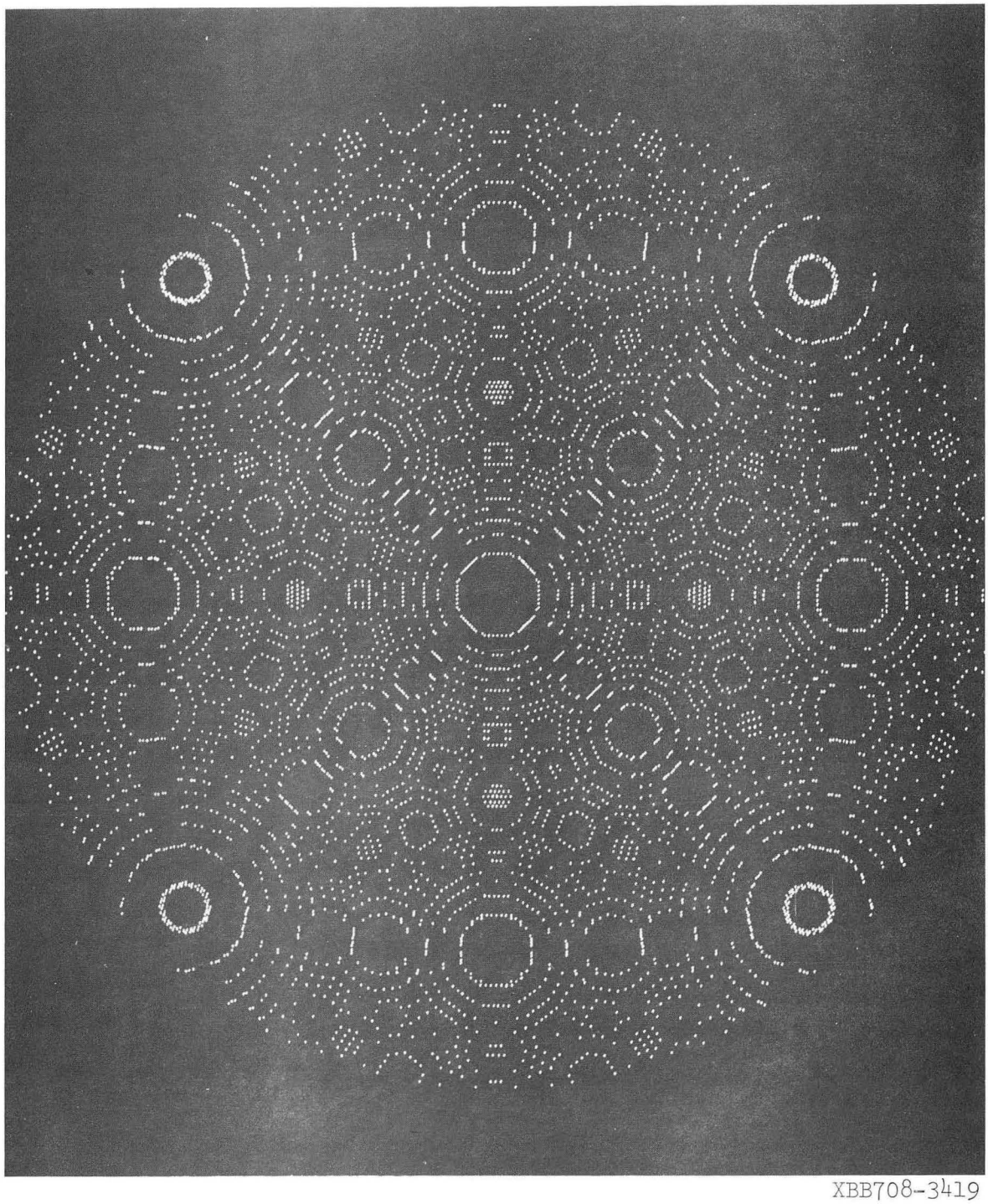

XBB708-3419

Fig. 16.

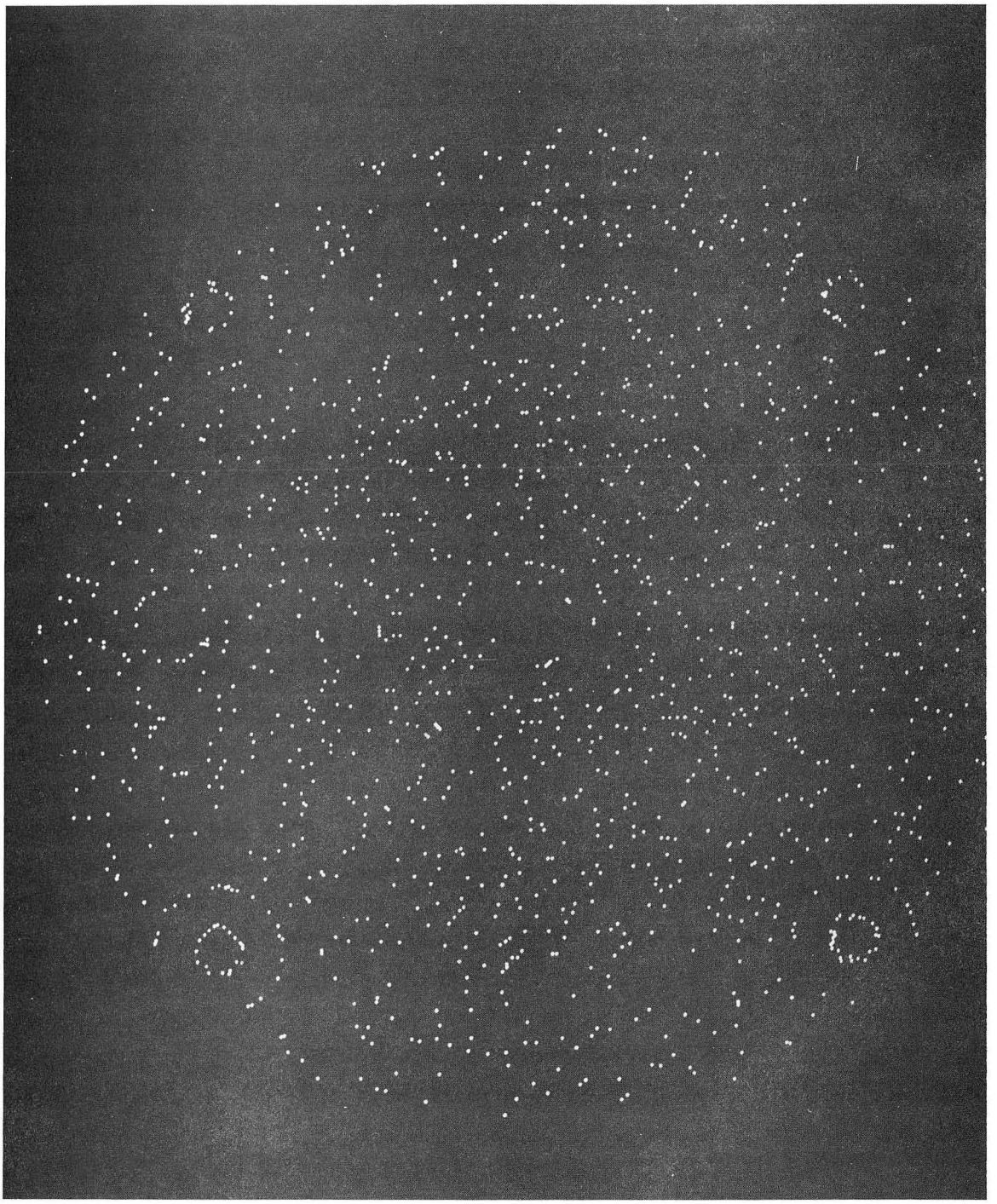

XBB708-3420

Fig. 17.

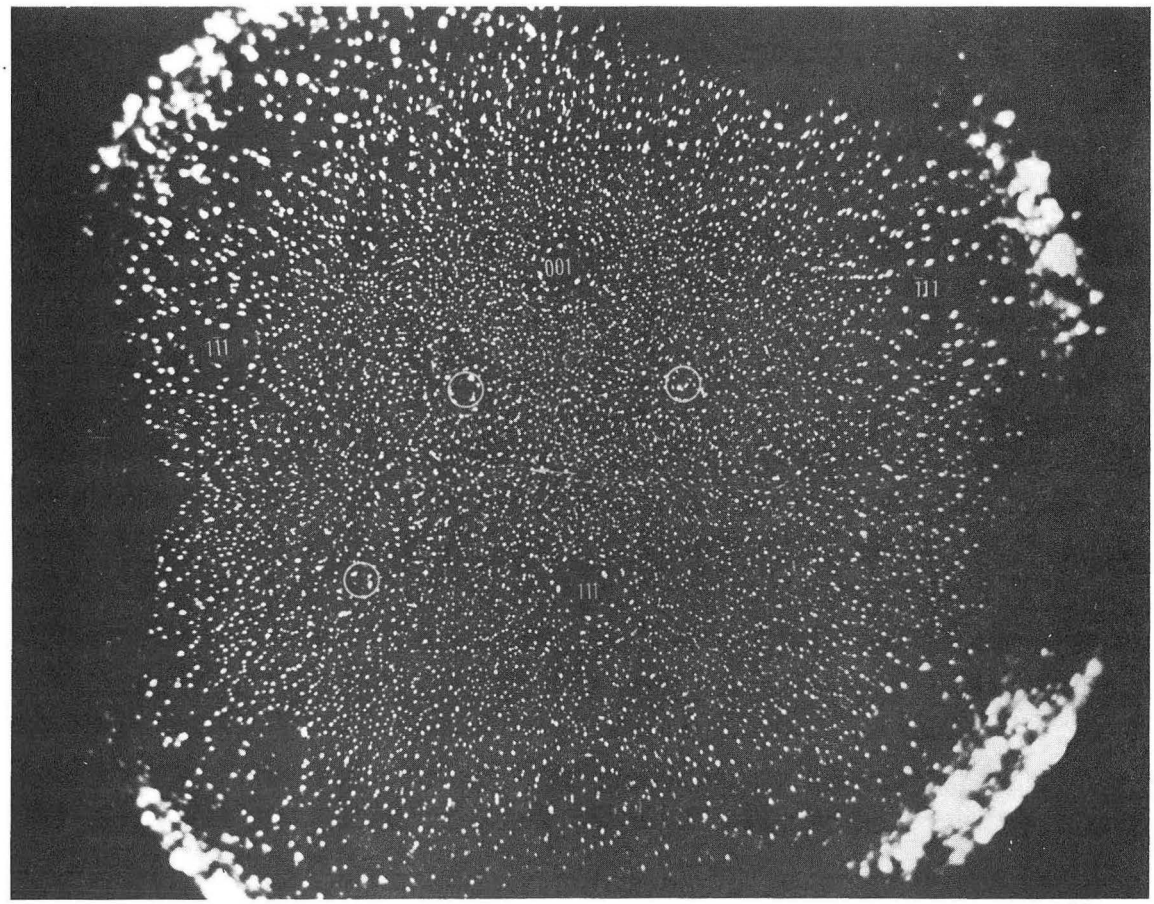

XBB7010-4497

Fig. 18.

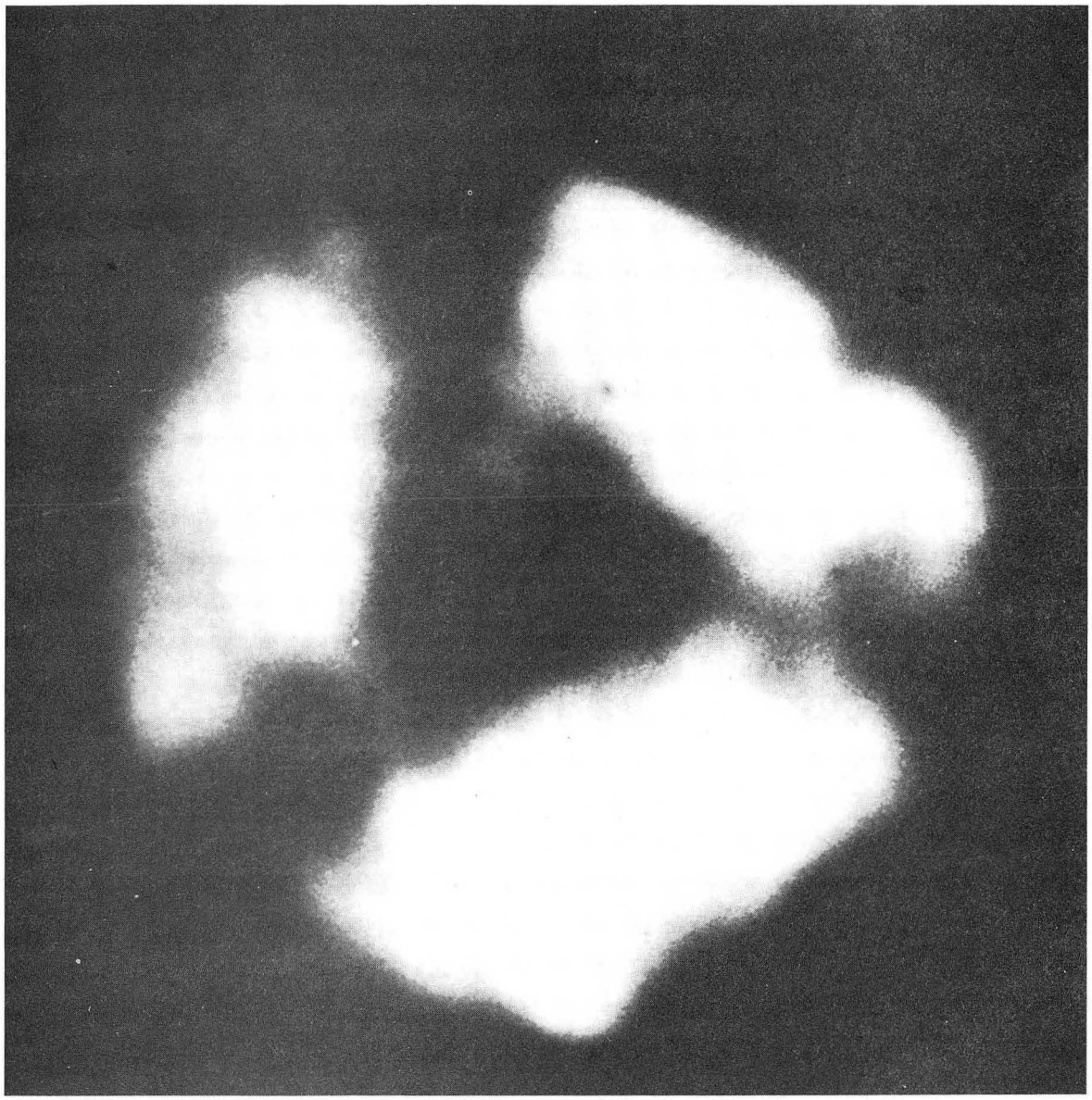

XBB7012-5565

Fig. 19.

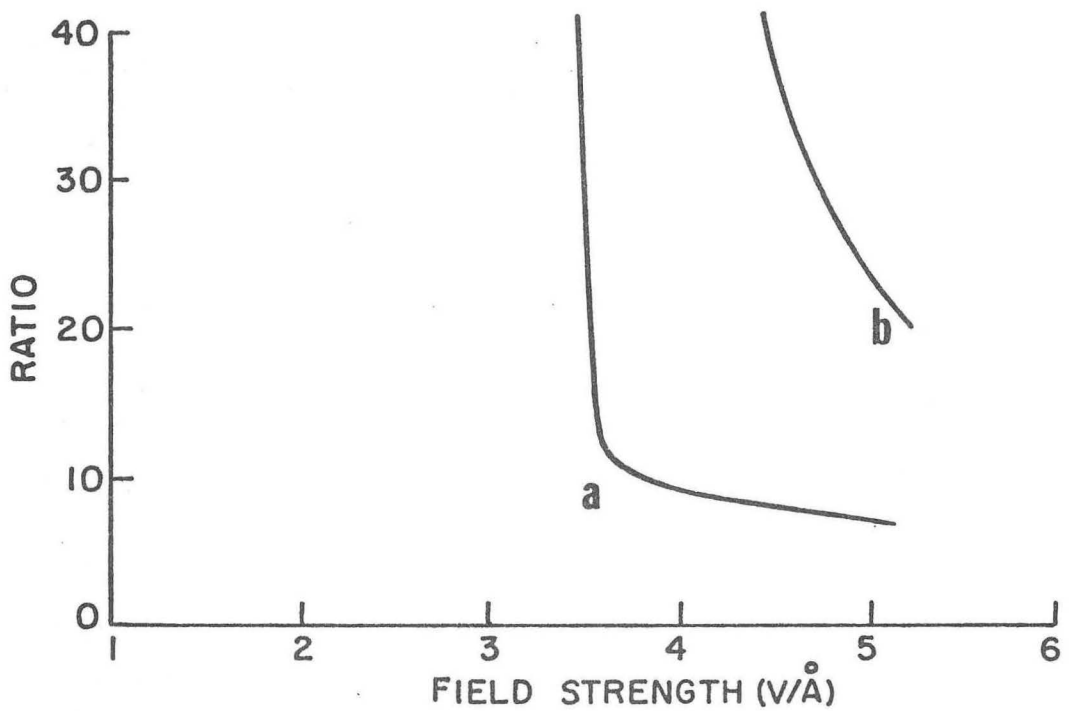

XBL 7012-7368

Fig. 20.

LEGAL NOTICE